J. Fluid Mech. (2010), *vol.* 658, *pp.* 509–538.
doi:10.1017/S0022112010002375

Linear and nonlinear mechanisms of sound radiation by instability waves in subsonic jets

VICTORIA SUPONITSKY[1]†, NEIL D. SANDHAM[1] AND CHRISTOPHER L. MORFEY[2]

[1]School of Engineering Sciences, University of Southampton, Southampton SO17 1BJ, UK

[2]ISVR, University of Southampton, Southampton SO17 1BJ, UK

(Received 23 July 2009; revised 16 April 2010; accepted 18 April 2010; first published online 30 June 2010)

Linear and nonlinear mechanisms of sound generation in subsonic jets are investigated by numerical simulations of the compressible Navier–Stokes equations. The main goal is to demonstrate that low-frequency waves resulting from nonlinear interaction between primary, highly amplified, instability waves can be efficient sound radiators in subsonic jets. The current approach allows linear, weakly nonlinear and highly nonlinear mechanisms to be distinguished. It is demonstrated that low-frequency waves resulting from nonlinear interaction are more efficient in radiating sound when compared to linear instability waves radiating directly at the same frequencies. The results show that low-frequency sound radiated predominantly in the downstream direction and characterized by a broadband spectral peak near $St = 0.2$ can be observed in the simulations and described in terms of the nonlinear interaction model. It is also shown that coherent low-frequency sound radiated at higher angles to the jet axis ($\theta = 60°$–$70°$) is likely to come from the interaction between two helical modes with azimuthal wavenumbers $n = \pm 1$. High-frequency noise in both downstream and side-line directions seems to originate from the breakdown of the jet into smaller structures.

Key words: aeroacoustics, jet noise, nonlinear instability

1. Introduction

It is generally recognized that large-scale organized structures (sometimes modelled as linear instability waves) play an important role in the generation of noise from jets. In supersonic jets a mechanism is readily identified since the most unstable waves in the jet column have a nominally supersonic phase velocity and are able to radiate sound efficiently (see e.g. Tam & Burton 1984; Wu 2005). In subsonic jets the situation is less clear and, although experimental studies support the idea that radiated sound is connected to hydrodynamic wavepackets within the jet, the detailed mechanisms that generate suitable wavepackets are not well understood. There can be a linear connection between the dominant instability modes in the initial region and the far-field sound, as in supersonic jets; but as we shall see later, this does not explain the presence in subsonic jets of a broadband spectral peak near $St = 0.2$ at angles of around 30° to the jet axis (e.g. Stromberg, McLaughlin & Troutt 1980; Viswanathan 2004, 2008). There can also be a nonlinear process, as was clearly

† Email address for correspondence: v.suponitsky@soton.ac.uk

demonstrated in the little-known experimental study of Ronneberger & Ackermann (1979), in which a fully turbulent subsonic jet was perturbed with plane acoustic waves transmitted through the nozzle from upstream. Simultaneous forcing at two frequencies (e.g. $St_1 = 0.5$ and $St_2 = 0.3$ in one experiment and $St_1 = 0.7$ and $St_2 = 0.5$ in another) produced a measurable pressure signal in the acoustic far field at the difference frequency $St_1 - St_2 = 0.2$, amplified by as much as 30 dB relative to the same acoustic forcing with zero flow. The authors interpreted their results in terms of a nonlinear interaction between waves at the two forcing frequencies, driving a spatially modulated wavepacket with associated sound radiation. A simple physical argument for the latter process is that although the wavepacket has a local phase speed that is subsonic, a Fourier transform of a suitable variable in the streamwise direction will lead to a broadband wavenumber spectrum, a portion of which will be supersonic relative to the ambient and hence able to radiate as Mach waves (e.g. Tam & Morris 1980; Tam 2009).

This study is aimed at providing further physical insight into the role of instability waves in the sound radiation from subsonic jets. A method based on numerical simulations will be presented that can distinguish between the linear and nonlinear (wave interaction) mechanisms on the basis of their dependence on forcing amplitude. In particular, it will be shown that some important features of subsonic jet noise that are observed in experimental measurements, particularly near the spectral peak in the dominant radiation direction, can be replicated by forcing a prescribed steady base flow with a flat spectrum of instability waves, of sufficient amplitude for nonlinear interactions to occur.

1.1. *Previous experimental investigations*

Several investigators besides Ronneberger & Ackermann (1979) carried out experiments on subsonic jets (both forced and unforced) relevant to the issue outlined above. Moore (1977) studied sound radiation from natural and forced air jets at model scale (nozzle diameter $D = 39$ mm), covering the Mach number range $M = 0.1$–0.9 based on jet centreline velocity U_j and ambient sound speed. In order to establish whether instability waves cause a turbulent jet to act as an amplifier of single-frequency acoustic disturbances that are transmitted through the nozzle, Moore (1977) placed an acoustic source in the upstream plenum of his jet rig. Under single-frequency forcing at f_0, the measured near-field response of the jet was found to be consistent with linear instability mode predictions based on the local mean velocity profile. However, comparisons of the net acoustic power travelling down the jet pipe with the power radiated at f_0 into the far field showed no significant amplification, over the range of the experiments ($M < 0.9$, $St_0 > 0.18$ with $St_0 = f_0 D/U_j$). These results led Moore to conclude that instability waves in natural turbulent jets do not contribute directly to far-field radiation, in contrast to the supersonic case described by Tam & Burton (1984). Considered from the perspective of the Ronneberger & Ackermann (1979) study, this is perhaps not surprising, since Moore's single-frequency study omitted wave interactions. The simulations presented in § 3 will address this issue directly.

Moore's conclusion was also challenged by Laufer & Yen (1983), based on measurements of natural and forced instability waves in the first diameter of a low-subsonic jet ($M = 0.05$–0.2). Laufer & Yen (1983) were able to achieve an exceptionally low turbulence intensity at the exit of their nozzle (less than 0.1 %), together with a laminar initial shear layer; these features combined with the relatively low Reynolds number ($Re = (0.6\text{–}2.3) \times 10^5$) to produce a rather well-ordered initial region in which the most unstable frequency of the exit shear layer, f_0, appeared prominently in the

near-field pressure spectrum along with its first and second subharmonics (f_1, f_2). When the jet was forced acoustically via an annular slot surrounding the nozzle lip, the spectral peaks increased in amplitude and became sharper. It should be noted that the corresponding fundamental Strouhal number St_0 was 4.3–8.5; thus, there is no overlap in the Strouhal number with the experiments of Moore (1977). It is also worth mentioning that the acoustic forcing was intended to be axisymmetric. However, this would have been difficult to ensure in practice, because the acoustic wavelength at f_0 was less than the nozzle circumference at all Mach numbers except the lowest.

Notable features of the Laufer & Yen (1983) results are: (i) the axial locations of the r.m.s pressure maxima at f_n ($n = 1, 2$), measured along a 10° line from the nozzle lip, correspond to the source locations for 30° far-field radiation at each frequency; (ii) the near-field pressure and velocity maxima at f_n vary almost linearly with forcing amplitude ($n = 0, 1, 2$), as does the fundamental far-field pressure; but (iii) the subharmonic far-field pressures at 30° to the axis ($n = 1, 2$) vary quadratically with the corresponding velocity maxima (see figure 39) and hence approximately as the square of the forcing amplitude, indicating a quadratic nonlinear mechanism.

Experimental results of Stromberg *et al.* (1980) for a subsonic low-Reynolds-number jet ($Re = 3600$, $M = 0.9$) also indicate that a nonlinear mechanism involving the dominant $St \approx 0.44$ instability waves is responsible for a significant portion of the peak noise generated from this transitional jet (around $St \approx 0.22$); however, the authors speculated that vortex pairing is responsible. It is worth noting that direct numerical simulation (DNS) of the subsonic jet for the same flow parameters as in Stromberg *et al.* (1980) was carried out by Freund (2001) and the radiated sound was calculated using Lighthill's acoustic analogy. The results showed very good agreement with the experimental data of Stromberg *et al.* (1980).

In a careful series of far-field noise measurements on fully turbulent jets, Viswanathan (2004, 2008) observed the typical spectral shape associated with large-scale turbulence (e.g. Tam & Golebiowski 1996) down to very low Mach numbers ($M = 0.26$). At the lowest Mach numbers this spectrum shape was observed only at angles close to the jet downstream axis, while with increasing Mach number it extended to larger angles. To explain these results, Viswanathan (2008) suggested that as a consequence of spatial modulation of the instability wave amplitude due to the growth/decay cycle, low-wavenumber components with supersonic phase speeds relative to the ambient speed of sound could be present. These would radiate into the far field, but because of their low phase speed (only just supersonic) the radiation would be confined to angles close to the jet axis. Tam *et al.* (2008) give a similar explanation; their paper provides further experimental evidence of the connection between large-scale turbulent structures and jet noise in the downstream sector.

1.2. *Theoretical and computational models*

Recently, there have been a number of studies proposing simplified models of the sound radiation from subsonic jets. Models based on weakly nonlinear instability mode interactions have been proposed by Sandham, Morfey & Hu (2006*a*). A plane parallel jet flow was subjected to a spatially localized initial disturbance and DNS showed sound radiation starting from an early stage of nonlinear development. In an attempt to reproduce the sound radiation pattern obtained by DNS, two simplified models were proposed. The first model consists of a pair of linearized Euler equations, where the second depends on the output of the first and nonlinearities are explicitly included as forcing terms in the second linear system. Linearized Euler equations are

first solved for the strictly linear response to the same initial conditions as in the DNS calculations. Forcing terms $f_i = -\partial(u_i u_j)/\partial x_j$ (taken according to the Lilley–Goldstein acoustic analogy, e.g. Goldstein 2001) are then calculated from the solution obtained. An inhomogeneous linear problem is then solved to find the response to the nonlinear forcing. In the second model, the linear response and forcing terms are constructed using eigenvalues and eigenfunctions from temporal linear stability theory. The results obtained with such models showed encouraging agreement with those obtained from DNS. A detailed examination of the source terms suggested that the 'difference-wavenumber mode', arising from the nonlinear interaction between instability waves, dominates far-field sound radiation from a subsonic jet.

In subsequent studies Sandham & Salgado (2008) extended the method of Sandham *et al.* (2006*a*) to spatially developing waves and round jets. In this study the parabolized stability equations (PSE) were used to calculate wavenumbers and mode shapes of the specified spatially developing base flow. The sound radiation from the various mode interactions was then found by solving a Lilley–Goldstein wave equation. The method was applied to a round single-stream jet for which experimental and DNS results are available (Stromberg *et al.* 1980; Freund 2001). The results obtained with regard to the most amplified frequency in the near field and the dominant frequency of the sound radiation in the far field were in close correspondence with the experimental and DNS data, further suggesting that the simplified model is able to capture some of the important mechanisms of the subsonic jet noise.

In a recent theoretical study Wu & Huerre (2009) focused on the sound generated by a pair of helical instability waves with nearly the same frequency and opposite azimuthal wavenumbers, using a matched-asymptotic-expansion approach. According to their model, a 'streaming' effect of the wave interaction generates a strong slowly breathing, azimuthally dependent 'mean flow distortion' that acts as an emitter of low-frequency sound. The sound field predicted by the above model is characterized by a single-lobed directivity pattern beamed at an angle about 45°–60° from the jet downstream axis, and a broadband spectrum centred at a Strouhal number $St \approx 0.07$–0.2.

1.3. *Present contribution*

In this study we use numerical simulations of the compressible Navier–Stokes equations to study how the nonlinear interaction between two instability modes leads to the generation of a 'difference-frequency' response that is likely to radiate into the far field and dominate the far-field radiation. Different kinds of nonlinear interactions are considered and an attempt is made to summarize likely contributions of particular interactions to the overall sound. The base flow is prescribed using the experimental data of Stromberg *et al.* (1980) and maintained during the calculations (see §2 for details). This approach allows us to distinguish between linear and nonlinear mechanisms of sound radiation by instability waves, and to isolate this sound from that originating from smaller scale turbulence. This study aims to find answers to the following questions: (i) what part of the overall sound from subsonic jets comes from instability waves (large-scale structures) and (ii) how well do the simplified models proposed and studied by Sandham *et al.* (2006*a*) and Sandham & Salgado (2008) predict this part of the noise? The rest of this paper is organized as follows. The numerical approach and problem statement are given in §2. The results of exciting the jet by two primary instability waves are presented in §3, which is subdivided into §§3.1–3.3, each describing a specific nonlinear interaction. The

results of exciting the jet by a wide range of modes are given in § 4. Results are summarized in § 5.

2. Numerical approach

The compressible Navier–Stokes equations for the conservative variables are solved using a finite-difference DNS code. The convection and diffusive terms are evaluated by a fourth-order-accurate central scheme using a five-point stencil, while time marching is achieved by a third-order explicit Runge–Kutta scheme. No artificial viscosity or filtering is used, and the stability of the code is enhanced by entropy splitting of the inviscid flux terms together with a Laplacian formulation of the viscous terms (Sandham, Li & Yee 2002). The code has previously been used in a number of published studies (e.g. Sandham *et al.* 2002; Sandberg, Sandham & Joseph 2007; Jones, Sandberg & Sandham 2008) and has been validated extensively.

Simulations of a subsonic round jet were performed on a Cartesian grid. The dimensions of the computational box in the streamwise (z) and normal (x, y) directions were varied depending on the wavelength of the radiated sound (this will be discussed in the results section); however, the grid resolution (Δx, Δy and Δz) was kept the same for all simulations. This size of the computational domain is enough to include some portion of the sound field. A uniform grid was used in the streamwise direction z with $\Delta z = 0.04545D$, where D is the jet diameter. In the directions normal to the flow (x and y) the grid spacing was $\Delta x = \Delta y = 0.02635D$ in the region close to the jet centreline. The resolution away from the jet core was gradually reduced to $\Delta x = \Delta y = 0.2108D$, which was found to be sufficient to resolve the acoustic waves. Numerical resolution has been examined by doubling the number of grid points in the transverse directions x and y (grid spacing of $\Delta x = \Delta y = 0.013175D$ near the jet centreline and $\Delta x = \Delta y = 0.1054D$ in the acoustic field). The results showed that increasing the resolution had no effect on the investigated physical phenomena, although some differences were observed in the radial profiles of the disturbances near the lip line $r/D = 0.5$ in the vicinity of the nozzle exit ($z \leqslant 2D$). In the acoustic field, the only effect of the resolution is a small change in the amplitude of the spectral peaks (changes of less than 10 %). Since the noise is mainly generated some distance downstream of the nozzle, the differences observed in the close vicinity of the nozzle exit have only a small effect on the radiated noise.

To check the effect of the domain size on the pressure sound field (in particular for the very low frequency waves), the computational domain was extended to $47D$ in the transverse direction (y) and to $50D$ in the streamwise direction (z). The observed differences in the pressure in the acoustic field were smaller than 1 %.

An integral boundary condition (Sandhu & Sandham 1994) was applied at the inflow boundary. This boundary condition allows a slight adjustment of the prescribed inflow profile in order to let small-amplitude acoustic disturbances pass through the boundary and leave the computational domain. Characteristic boundary conditions (Thompson 1987) were used at the outer boundaries in directions normal to the flow. A zonal characteristic boundary condition (Sandberg & Sandham 2006) was applied at the outflow boundary to reduce reflections occurring because of vortical structures passing through the boundary.

As mentioned earlier, a base flow field is prescribed by imposing time-independent forcing terms. In the absence of disturbances the base flow is maintained during the simulations. With such a formulation we follow the spatial evolution of disturbances (taken as a sum of instability waves) on the base flow. When the inflow disturbance is

of sufficiently small amplitude, the current formulation converges to that of a linear stability analysis, as the influence of nonlinear terms is negligible. Therefore, the results obtained can be directly compared with those obtained from linear stability theory (LST) for parallel base flows or PSE (to include non-parallel effects). On the other hand, when the amplitude of the inflow disturbance becomes significant, the nonlinear interactions between instability waves can be examined along with the resulting sound. In this case, the effect of mean flow distortion is included in the simulations.

The application of stability analysis to several kinds of free shear flows including turbulent mixing layers is known to have a high degree of success (Crighton & Gaster 1976; Gaster, Kit & Wygnanski 1985). In such flows the instability mechanism is mainly controlled by the mean–velocity profiles. The fine-scale turbulence behaves approximately as an added 'eddy' viscosity on the averaged and large-scale motions; for details see Gaster *et al.* (1985). Therefore, relying on the assumption that the influence of small-scale turbulence on large-scale structures is small, this kind of analysis is expected to be suitable for fully turbulent jets also. Experimental evidence of the existence of instability waves in a subsonic turbulent round jet can be found in a recent work by Suzuki & Colonius (2006).

In our simulations the base flow has been chosen to match the experimental data of Stromberg *et al.* (1980), obtained for a single-stream transitional subsonic jet with Mach number 0.9 and Reynolds number of 3600. The same base flow was used in previous studies by Sandham & Salgado (2008) and Sandham, Salgado & Agarwal (2008). It is worth noting that the results obtained with the current approach are sensitive to the base flow. The basic mechanisms, however, are expected to remain unchanged.

The streamwise velocity of the base flow at any streamwise position z and radial position r is given by

$$\overline{V}_z = 0.5\left[\tanh\left(\frac{r+a}{\delta}\right) - \tanh\left(\frac{r-a}{\delta}\right)\right], \quad z > 0, \tag{2.1}$$

with empirically determined parameters

$$a = 0.59 + 0.09\,\tanh(\sqrt{z} - 2.9), \quad \delta = \frac{39 + 24z + 0.11z^4}{1000 + z^3}. \tag{2.2}$$

A weak co-flow is added to the streamwise velocity component to allow a proper functioning of the characteristic boundary conditions. Therefore, in the simulations the velocity profile given by (2.1) was adjusted to

$$\overline{V}_z^{sim} = (\overline{V}_z + v_{coflow})/(\overline{V}_z(r=0, z=0) + v_{coflow}). \tag{2.3}$$

Typically, $v_{coflow} = 1\,\%$. The base flow radial velocity component is set to zero in the simulations, although it can be computed from the continuity equation. Preliminary tests were conducted with the radial velocity component computed from the continuity equation and showed little difference. No swirl is added to the jet; so the mean azimuthal component $\overline{V_\theta}$ is set to zero. The pressure of the base flow is assumed to be uniform. The temperature of the jet at $z = 0$ is assumed to be the same as the surrounding temperature, and the profile further downstream is approximated using a Crocco–Busemann relation

$$\overline{T} = 1 + \frac{\gamma - 1}{2} M^2 \overline{V}_z^{sim}\left(1 - \overline{V}_z^{sim}\right). \tag{2.4}$$

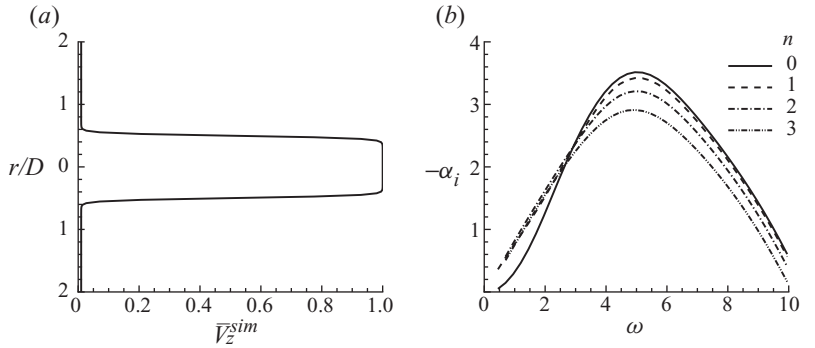

FIGURE 1. (*a*) Inflow velocity profile given by (2.3) for $z=0$ and $v_{coflow}=0.01$; (*b*) growth rates $-\alpha_i$ for the first few azimuthal modes calculated from the linear stability theory.

In order to maintain the above base flow, corresponding source terms were added to the right-hand side of the Navier–Stokes equations.

Disturbances are taken in the form of normal modes at the inflow boundary

$$\tilde{u} = \mathrm{Re}\{A\hat{u}(r)\exp(\mathrm{i}(n\Theta - \omega t + \phi))\}, \tag{2.5}$$

where Re defines the real part, A is the amplitude of the mode, $\hat{u}(r)$ is an eigenfunction (shape of the mode), n is the azimuthal mode number, ω is a real angular frequency and ϕ is the phase. Eigenfunctions and wavenumbers are obtained from spatial linear stability analysis (solution of the compressible Orr–Sommerfeld equation) for a particular frequency and mode number. Disturbances are added to all flow variables at the inflow boundary.

In the equations above (and also in the results in § 4), all variables are normalized by the diameter of the jet and the jet centreline velocity at the nozzle exit. In (2.5) the eigenfunctions $\hat{u}(r)$ are normalized such that the peak amplitude of the streamwise velocity fluctuations is equal to 1.

3. Sound radiation from the jet excited by a combination of two instability waves

We start with a detailed examination of the sound field generated by perturbing the jet with a combination of two highly amplified instability waves of different frequencies. Each of the following subsections is devoted to the results obtained for the jet excited with different combinations of azimuthal mode numbers. The main goal of the first part of the results is to investigate whether the difference frequency arising from the nonlinear interaction between two waves is indeed active in the acoustic field and dominates sound radiation from jets, as was suggested in previous simplified studies (Sandham *et al.* 2006*a*; Sandham & Salgado 2008). Simulations were performed for $M=0.9$, $Re=3600$ and $v_{coflow}=0.01$. The inflow velocity profile given by (2.3) is shown in figure 1(*a*), and growth rates of the first few azimuthal modes corresponding to this profile and calculated from LST are shown in figure 1(*b*).

3.1. *Interaction between two axisymmetric modes (0/0 interaction)*

In this section the sound field generated by a combination of two axisymmetric waves of different frequencies is studied ($n_1=n_2=0$). The length of the computational domain in the streamwise direction z was $30D$, followed by an outflow zone of $20D$ length in which the grid was stretched by a factor of 2. The computational domain

Case	ω_1	n_1	ω_2	n_2	$\Delta\omega$	Δn	A	Mag. factor	p_{rms} $(z/D=0, r/D=0.5)$	$(p_{rms})_{max}$
$A1$	2.2	0	3.4	0	1.2	0	5×10^{-6}	1	8.756×10^{-7}	1.52×10^{-4}
$A2$	2.2	0	3.4	0	1.2	0	1×10^{-5}	2	1.751×10^{-6}	3.04×10^{-4}
$A3$	2.2	0	3.4	0	1.2	0	1×10^{-4}	20	1.751×10^{-5}	3.04×10^{-3}
$A4$	2.2	0	3.4	0	1.2	0	5×10^{-4}	100	8.756×10^{-5}	1.42×10^{-2}
$A5$	2.2	0	3.4	0	1.2	0	1×10^{-3}	200	1.75×10^{-4}	2.5×10^{-2}
$D1$	2.2	0	2.8	0	0.6	0	5×10^{-4}	–	–	–
$D2$	2.6	0	2.8	0	0.2	0	5×10^{-4}	–	–	–
$D3$	2.6	0	2.8	0	0.2	0	1×10^{-4}	–	–	–
$P1a$	2.2	0	3.3	0	1.1	0	1×10^{-4}	–	–	–
$P1b$	2.2	0	3.3	0	1.1	0	5×10^{-4}	–	–	–
$P2a$	1.4	0	2.8	0	1.4	0	1×10^{-4}	–	–	–
$P2b$	1.4	0	2.8	0	1.4	0	5×10^{-4}	–	–	–
$S1$	1.2	0	–	–	–	–	1×10^{-3}	–	–	–
$S2$	1.2	0	–	–	–	–	1×10^{-4}	–	–	–

TABLE 1. Inflow disturbance characteristics.

was extended from $-15D$ to $15D$ in the transverse direction x and from $-15D$ to $25D$ in the transverse direction y. Simulations were carried out for different amplitudes and frequencies of the inflow disturbances as listed in table 1.

3.1.1. *Effect of the inflow disturbance amplitude*

Here we examine the effect of the disturbance amplitude (which controls the 'degree of nonlinearity' reached by the disturbances at the point of maximum amplification) on the radiated sound. To achieve this, the flow is perturbed by two axisymmetric waves with frequencies $\omega_1=2.2$ and $\omega_2=3.4$, for a range of initial amplitudes. The frequencies ω_1 and ω_2 were chosen so that the difference frequency resulting from nonlinear interaction between two waves would be maximally amplified. These frequencies were chosen based on linear PSE; details can be found in Sandham & Salgado (2008). Simulations for five different amplitudes of the inflow disturbance were carried out (cases $A1$–$A5$ in table 1). The two primary waves have the same amplitude A (2.5), given in the eighth column of table 1, and zero phase difference. The last two columns of the table give the pressure r.m.s. value of the inflow disturbance in the shear layer at $r/D=0.5$, and the streamwise maximum value of the r.m.s. pressure (located near the end of the potential core) obtained for the particular amplitude of inflow disturbance. The maximum r.m.s. value serves as a measure of the nonlinearity experienced by the disturbance when it reaches its maximum magnitude.

Figure 2 shows the instantaneous dilatation rate field obtained for different amplitudes of the inflow disturbance (results for cases $A1$ and $A2$ are very similar; so we show the results for only one of these cases). In the case of a very low amplitude (figure 2*a*), the disturbance magnitude does not reach values sufficient to cause observable nonlinear interactions before the disturbance starts to decay because of the jet spreading. In this case, only the sound generated by the instability wave itself (i.e. the direct linear mechanism of sound generation) can be observed. The acoustic wavelength λ_1 corresponds to the lower inflow forcing frequency $\omega_1=2.2$, which undergoes stronger amplification during the disturbance evolution. We can also see that the sound radiated by the linear mechanism (similar to that of Mach wave radiation in highly supersonic jets) is highly directional and confined to small angles from the jet downstream axis.

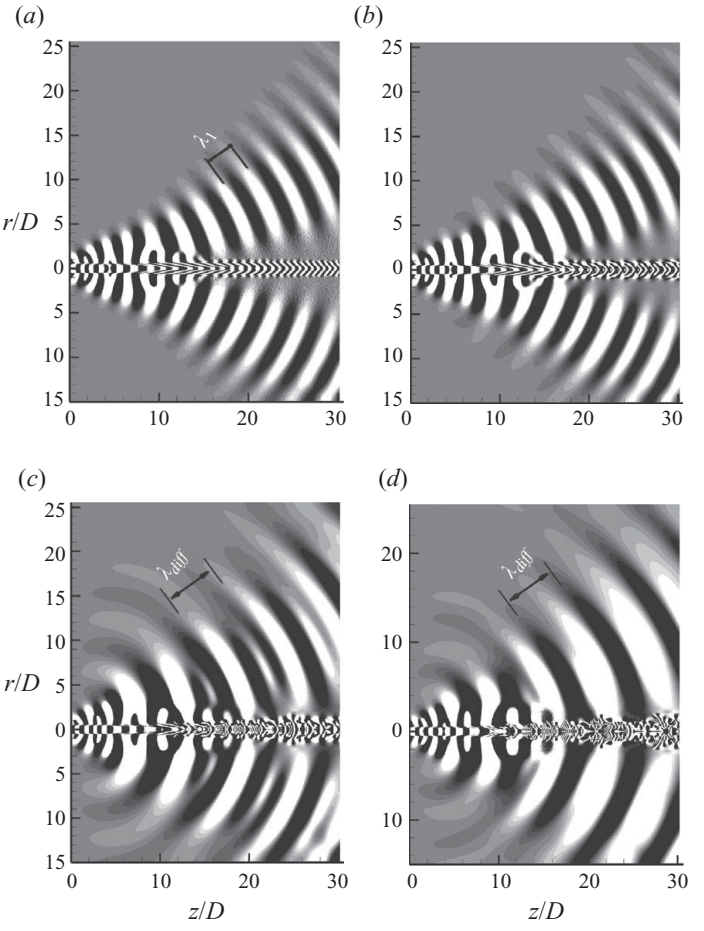

FIGURE 2. Dilatation rate contours obtained by perturbing the jet with two axisymmetric modes at frequencies $\omega_1 = 2.2$ and $\omega_2 = 3.4$. Results are shown for four different amplitudes of the inflow disturbance given in table 1 (cases *A*2–*A*5). (*a*) $A = 1 \times 10^{-5}$ (contour levels: -2×10^{-7} to 2×10^{-7}); (*b*) $A = 1 \times 10^{-4}$ (-2×10^{-6} to 2×10^{-6}); (*c*) $A = 5 \times 10^{-4}$ (-1×10^{-5} to 1×10^{-5}); (*d*) $A = 1 \times 10^{-3}$ (-2×10^{-5} to 2×10^{-5}). λ_1 and λ_{diff} correspond to the dominant acoustic wavelength for the linear and nonlinear mechanisms, respectively.

With increasing disturbance amplitude (figure 2*b–d*), nonlinear interactions become more and more significant. As a result, a change in the structure of the sound field can be observed. In case *A*3 (figure 2*b*), the acoustic field still seems to be dominated by linear sound, although the appearance of other frequencies can also be noticed. For higher amplitudes (figure 2*c*,*d*) an increase in the wavelength of the emitted sound (λ_{diff}) is seen, and in these cases the dominant frequency corresponds to that of the difference frequency mode $\Delta\omega = 1.2$. It is also noticeable that the decay of the disturbance amplitude further downstream is much slower when nonlinear interactions are significant. This is probably because the lower frequencies resulting from these interactions continue to be amplified further downstream. The sound generated by the nonlinear mechanism extends over a broader range of angles from the jet downstream axis in comparison to that radiated by the linear mechanism. Even then, the sound is still highly directional and is confined mainly to angles less than 45° from the jet downstream axis.

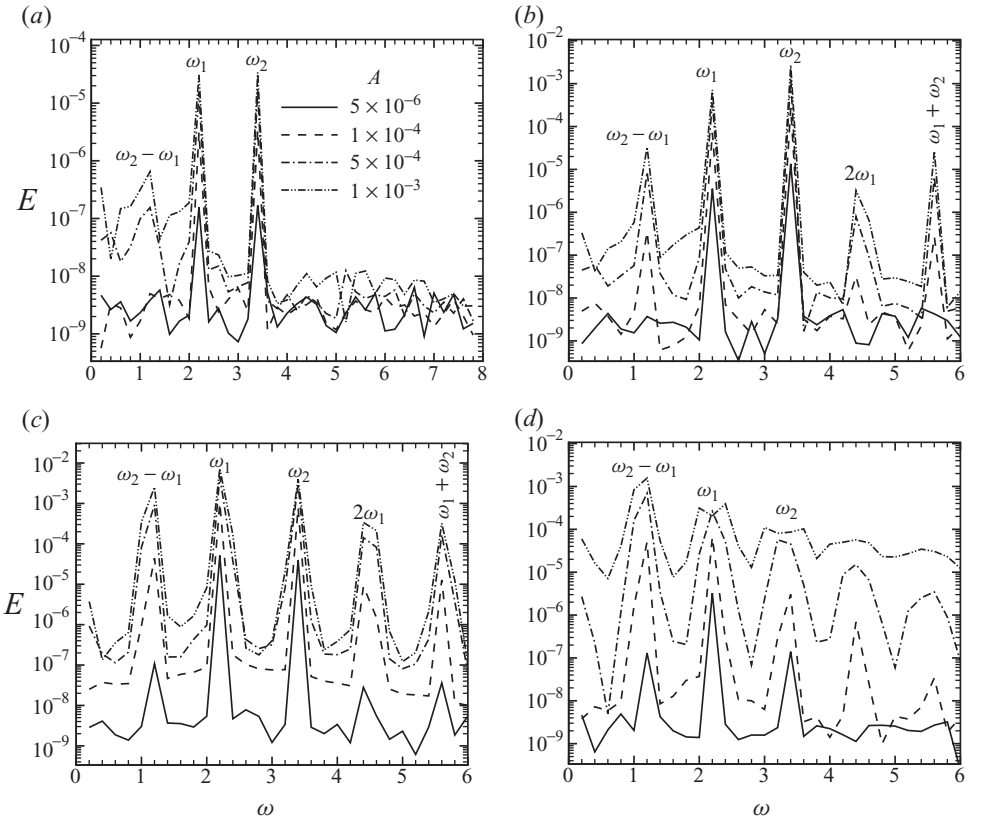

FIGURE 3. Spectra of pressure fluctuations in the shear layer at $r/D=0.7$ at different streamwise locations: (*a*) $z/D=0$; (*b*) $z/D=2$; (*c*) $z/D=5$; (*d*) $z/D=12$. Line styles are indicated in (*a*). Cases *A*1 and *A*3–*A*5.

The spectrum of pressure fluctuations (denoted by E) in the shear layer ($r/D=0.7$), at different streamwise locations and for different amplitudes of the inflow disturbances, is shown in figure 3. The length of the time-history signal used throughout the paper in spectra calculations is equal to one period of the lowest resolved frequency $\omega=0.2$. At $z/D=0$ (the nozzle exit), two spectral peaks of nearly equal power corresponding to the inflow frequencies $\omega_1=2.2$ and $\omega_2=3.4$ are seen. For larger amplitudes of the disturbance (the dash–dotted and dash–dot–dotted lines) the difference frequency $\Delta\omega=1.2$ can also be observed. At $z/D=2$, modes arising from various interactions (difference frequency, sum frequency and harmonics of ω_1 and ω_2) begin to be observed for all amplitudes of the inflow disturbance except for the smallest one (the solid line) for which the evolution process is still linear. Further downstream at $z/D=5$ the power of the difference mode becomes comparable to that of ω_1 and ω_2, and at $z/D=12$ it becomes the dominant mode, as all other higher frequency modes cease to be amplified at these streamwise locations.

Figure 4 shows the pressure fluctuations spectra on an arc of radius $25D$ centred at $z/D=0$ (the nozzle exit). The results are presented for four different amplitudes of the inflow disturbance (figure 4*a*–*d*) and for four different angles θ from the jet downstream axis. The difference frequency is the strongest signal in the acoustic field, when the amplitude of the inflow disturbance is sufficient to produce significant

$\Delta\omega = 1.2$	$\omega_1 = 2.2$	$\omega_2 = 3.4$	Ratio of inflow amplitudes
19.09	3.47	4.77	5

TABLE 2. Comparison of mode pressure amplitudes at $r = 25D$ and $\theta = 30°$: ratio between cases $A4$ and $A3$.

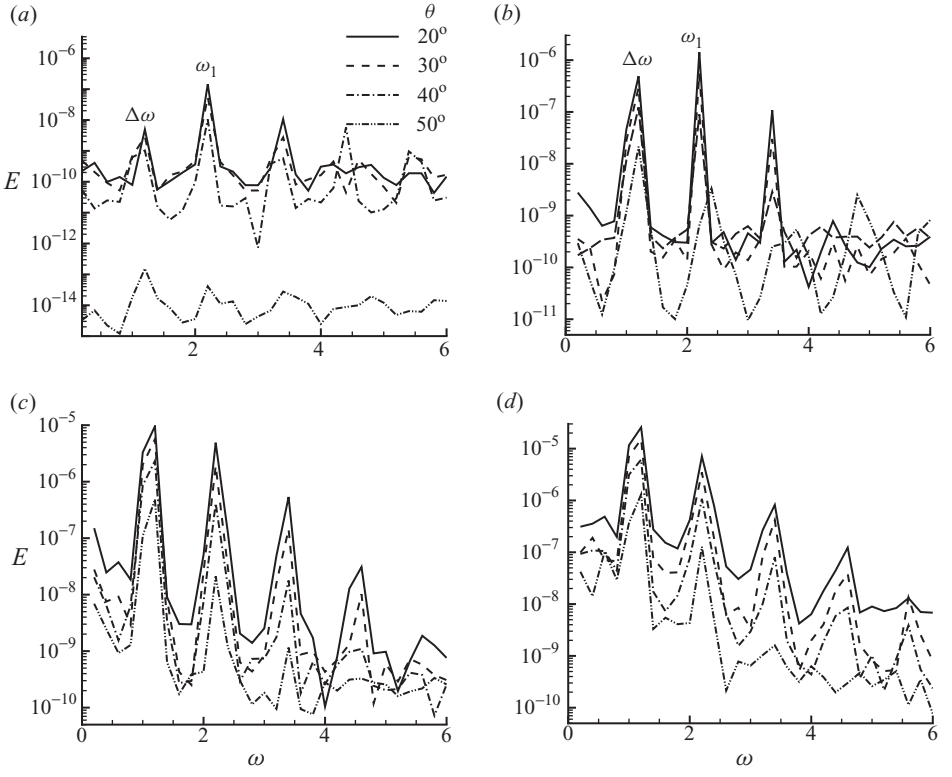

FIGURE 4. Pressure fluctuation spectra on an arc of radius equal to $25D$ centred at $z/D = 0$ (nozzle exit). (Here θ is the angle measured from the jet downstream axis.) Results are shown for four different amplitudes of the inflow disturbance given in table 1 (cases $A2$–$A5$). (*a*) $A = 1 \times 10^{-5}$; (*b*) $A = 1 \times 10^{-4}$; (*c*) $A = 5 \times 10^{-4}$; (*d*) $A = 1 \times 10^{-3}$. Line styles are indicated in (*a*).

nonlinear effects in the shear layer. The quadratic nonlinear nature of a spectral peak at the difference-frequency mode becomes apparent if we examine the increase in pressure amplitude of modes ω_1, ω_2 and $\Delta\omega$ as the inflow disturbance amplitude is increased. Results are shown in table 2 for comparison between cases $A3$ and $A4$. It can be seen that, while in the acoustic field the amplitude of the inflow frequencies varies approximately linearly with the disturbance amplitude, the amplitude of the difference mode varies approximately quadratically. (Note that nonlinear interactions also cause a slight change to the base flow as a result of Reynolds stresses; so the ratios are not exactly as expected.) The following conclusions can be drawn after examining the amplitude of the radiated sound at different angles from the jet downstream axis (sound directivity): (i) When sound is generated by the instability wave originally presented in the flow, i.e. by linear mechanism (e.g. at $\omega = 2.2$) there is a sharp cutoff of the sound at some angle θ. This can be seen clearly in

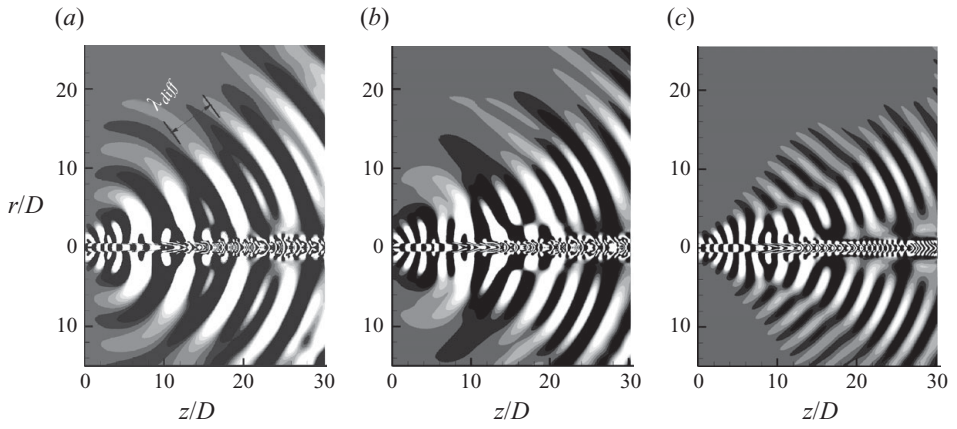

FIGURE 5. Dilatation rate contours obtained as a result of perturbing the jet by two axisymmetric modes with different $\Delta\omega$. Contour levels: -1×10^{-5} to 1×10^{-5}. (*a*) $\omega_1=2.2$, $\omega_2=3.4$, case *A*4; (*b*) $\omega_1=2.2$, $\omega_2=2.8$, case *D*1; (*c*) $\omega_1=2.6$, $\omega_2=2.8$, case *D*2.

figures 4(*a*) and 4(*b*). Weak radiation occurring at $\omega=2.2$ and $\theta=50^\circ$ for high disturbance amplitudes (figure 4*c*, *d*) is likely to originate from nonlinear interaction rather than from a linear mechanism. (ii) There is a rapid decrease in the amplitude of the radiated sound with increasing angle θ from the jet downstream axis for both linear and nonlinear mechanisms, but this decrease is slower in the case of the nonlinear mechanism. Therefore, the difference frequency is more prominent for higher angles θ. (iii) For cases where nonlinear effects are significant (figure 4*c*, *d*), an additional spectral peak at $\omega=1$ acquires a significant amplitude. This peak results from the subsequent nonlinear interaction between the difference frequency mode $\Delta\omega=1.2$ and the inflow frequency $\omega_1=2.2$.

3.1.2. *Behaviour as* $\Delta\omega\to0$

In the previous section the frequencies of the primary waves were chosen to give maximum amplification of the difference frequency. The results obtained were in good qualitative agreement with experiments (Stromberg *et al.* 1980), but the choice of frequencies requires further clarification. When the frequencies become close to each other, the amplitude of the difference frequency near the end of the potential core decreases, but the radiation efficiency increases because of the lower frequency of the difference mode. Results obtained with an earlier simplified model (Sandham & Salgado 2008) suggested that the latter effect is dominant and the difference-frequency radiation gets stronger as the two frequencies approach each other. This result was somewhat surprising and further clarification was sought in the present study. For this purpose, two additional simulations were carried out with closely spaced primary frequencies (cases *D*1 and *D*2 in table 1). These simulations were performed for the same amplitudes of the inflow disturbance as in case *A*4, such that nonlinear effects are expected to be significant.

Figure 5 shows instantaneous dilatation rate contours for the cases with different $\Delta\omega$. It can be seen that when the difference between input frequencies is reduced to $\Delta\omega=0.6$, the structure of the sound field resembles that obtained with $\Delta\omega=1.2$ (compare figures 5*a* and 5*b*). In both cases the dominant wavelength corresponds to the difference frequency, although some higher frequencies are also noticeable at angles close to the jet downstream axis for the case with $\Delta\omega=0.6$. Further reducing

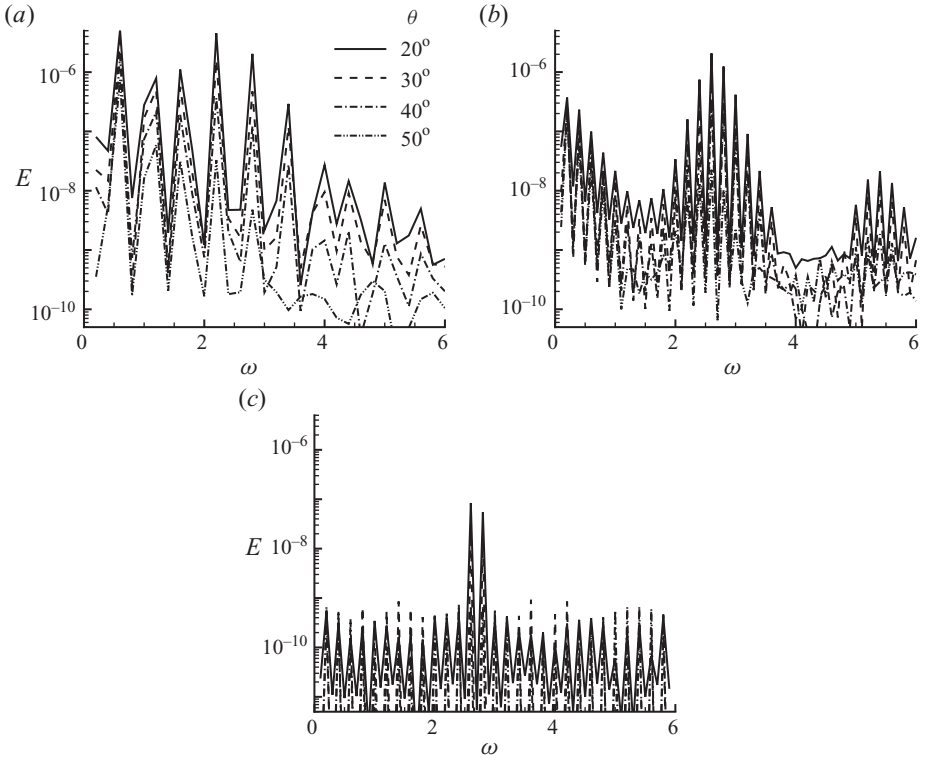

FIGURE 6. Pressure fluctuation spectra on an arc of radius equal to $25D$ centred at $z/D=0$ (nozzle exit). (Here θ is the angle measured from the jet downstream axis.) Results are shown for cases $D1$, $D2$ and $D3$ in table 1. (*a*) $\omega_1=2.2$, $\omega_2=2.8$, case $D1$; (*b*) $\omega_1=2.6$, $\omega_2=2.8$, case $D2$; (*c*) $\omega_1=2.6$, $\omega_2=2.8$, case $D3$. Line styles are indicated in (*a*).

the difference between frequencies to $\Delta\omega=0.2$ (figure 5*c*) leads to a change in the structure of the sound field. In this case, sound is mainly generated by the direct (linear) mechanism, and sound waves at the forcing frequencies (which are very close to each other) are observed.

Figure 6 shows the pressure fluctuations spectra on an arc of radius $25D$ at several angles θ from the jet downstream axis. Results are shown for cases $D1$ ($\Delta\omega=0.6$), $D2$ ($\Delta\omega=0.2$, $A=5\times10^{-4}$) and $D3$ ($\Delta\omega=0.2$, $A=1\times10^{-4}$) in figures 6(*a*), 6(*b*) and 6(*c*), respectively. It can be seen that, in general, the results for acoustic pressure obtained with $\Delta\omega=0.6$ (figure 6*a*) are similar to those obtained with $\Delta\omega=1.2$ (figure 3*c*). The difference frequency $\Delta\omega=0.6$ dominates the acoustic field at all angles θ, but its amplitude is slightly smaller than that obtained with $\Delta\omega=1.2$. When the two inflow frequencies are very close to each other (figure 6*b*), the spectra start to look different. In this case the very low frequency $\Delta\omega=0.2$ produced by nonlinear interaction between the two primary instability waves continues to interact with itself, creating a cascade of harmonics. In addition, it also interacts with each of the inflow frequencies generating additional modes in their vicinity. It seems that through these nonlinear processes, energy at the difference frequency $\Delta\omega=0.2$ is reduced. For the sake of completeness, spectra obtained for $\Delta\omega=0.2$ with very small inflow disturbance amplitude are shown in figure 6(*c*). One can see that for very small amplitude inflow disturbances, the linear mechanism is the dominant one and the sound field obtained

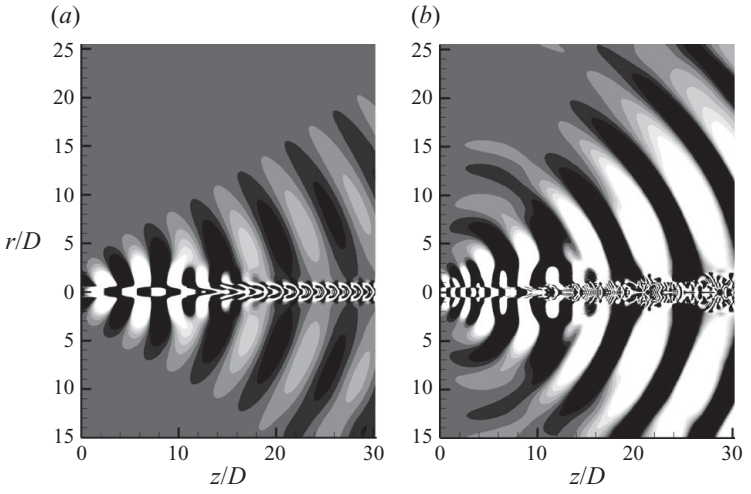

FIGURE 7. Dilatation rate contours. $A = 1 \times 10^{-3}$, contour levels -2×10^{-5} to 2×10^{-5}. (*a*) Jet perturbed by a single frequency $\omega = 1.2$, case $S1$ in table 1; (*b*) jet perturbed by two frequencies $\omega_1 = 2.2$ and $\omega_2 = 3.4$, case $A5$ in table 1.

is similar to the other cases with low amplitude inflow disturbance. To capture these effects in simplified models seems to require, as a minimum, nonlinear PSE with a large number of temporal modes.

3.1.3. *Remark on linear versus nonlinear mechanism of sound radiation*

In the previous sections we have demonstrated that for certain combinations of forcing frequencies, the difference frequency mode resulting from nonlinear hydrodynamic interactions can be an efficient direct sound radiator. This, in turn, may explain why acoustic spectra of subsonic jets have a broadband maximum at frequencies lower than those associated with the most unstable hydrodynamic modes near the end of the potential core. A logical question is: what happens if we perturb the jet by a single mode with a frequency equal to that of the difference frequency spectral peak? To clarify this issue we carried out two additional simulations in which the jet was perturbed by a single frequency $\omega = 1.2$ with two different amplitudes $A = 1 \times 10^{-3}$ and $A = 1 \times 10^{-4}$ (cases $S1$ and $S2$ in table 1). Results for these two cases show that the sound radiates at a single frequency $\omega = 1.2$ and its amplitude scales linearly with the amplitude of the inflow disturbance, indicating a linear radiation mechanism. Dilatation rate contours for cases $S1$ and $A5$ are compared in figures 7(*a*) and 7(*b*), respectively. The amplitudes of the forced modes are equal in both cases and the contour levels are the same. One can see that the nonlinear mechanism (figure 7*b*) is much more efficient in radiating sound in comparison to the direct (linear) mechanism (figure 7*a*).

In an attempt to explain what makes the nonlinear mechanism more efficient, the spatial envelope of the pressure at $\omega = 1.2$ was examined. A fast Fourier transform in time was performed for both simulations, and the pressure amplitude at $\omega = 1.2$ was extracted as a function of z at $r = 0.5D$ (see figure 8). At this point, it is worth recalling that the efficiency of sound radiation from subsonic modes is controlled by the following parameters (Crighton & Huerre 1990; Sandham, Morfey & Hu 2006*b*): (i) the frequency of the mode (radiation is more efficient for the lower frequencies), and (ii) the shape of the wavepacket (radiation is more efficient for the modes attaining

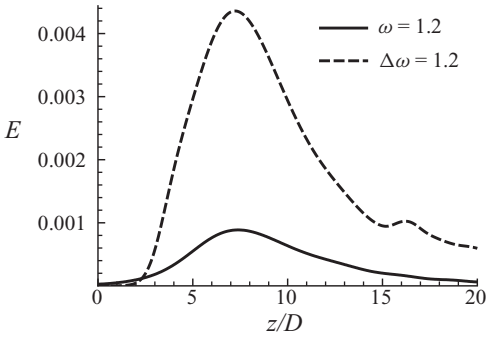

FIGURE 8. Axial variation of the mode amplitude corresponding to the frequency $\omega = 1.2$ (calculated from the pressure fluctuations inside the shear layer $r/D = 0.5$). Dashed line: two-frequency forcing (case $A5$; $\omega_1 = 2.2$; $\omega_2 = 3.4$); solid line: single-frequency forcing (case $S1$, $\omega = 1.2$).

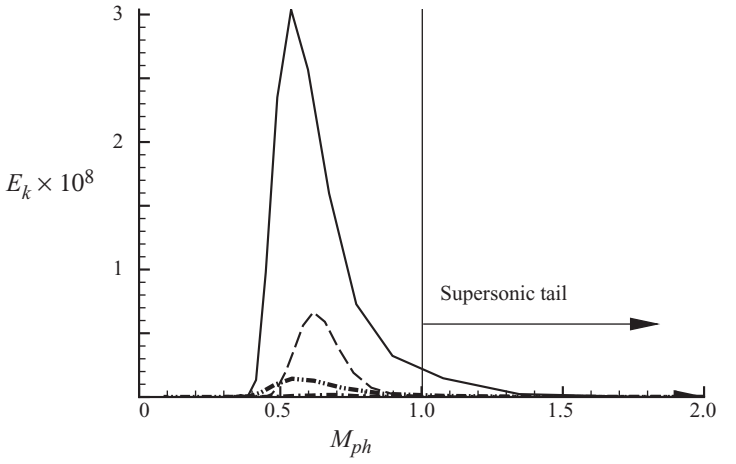

FIGURE 9. Wavenumber spectral energy (calculated from the pressure fluctuations) plotted against the phase Mach number M_{ph}. Spectra are shown at $r/D = 1.5$. Line codes for two-frequency forcing (case $A5$; $\omega_1 = 2.2$; $\omega_2 = 3.4$); solid line, $\Delta\omega = 1.2$; dashed line, $\omega_1 = 2.2$; dash-dotted line, $\omega_2 = 3.4$. Line code for single-frequency forcing (case $S1$): dash-dot-dotted line, $\omega = 1.2$.

rapid growth and saturation). By comparing the results in figure 8 one can see that while the frequency is the same, the shape of the wavepacket is different.

Further insight may be gained by examination of the energy content of wavenumber pressure spectra as only part of the spectra with supersonic phase velocities is potentially able to radiate sound into a far field (e.g. Tam & Morris 1980; Tam 2009). The wavenumber spectra are calculated by Fourier transform of pressure fluctuations in time and in the streamwise direction at a particular radial location. Figure 9 shows wavenumber spectra plotted against the phase Mach number $M_{ph} = C_{ph}/a$, where C_{ph} is a phase velocity and a is the ambient speed of sound. The phase velocity is given by $C_{ph} = \omega/k$, where k is the axial wavenumber. The spectra are shown at the radial distance $r/D = 1.5$. One can see that the difference frequency $\Delta\omega = 1.2$ (solid line) contains significantly more energy in the supersonic tail compared to spectra at the primary forcing frequencies ω_1 (dashed line) and ω_2 (dash-dotted line) and also

compared with spectra with excitation of the jet by a single frequency (dash-dot-dotted line). This illustrates why the difference frequency wave is more efficient in radiating sound compared with waves at the inflow frequencies. This also clarifies why the wave resulting from nonlinear interaction radiates sound more efficiently compared with the wave at the same frequency that is initially present in the flow. Finally, it is worth noting that the spectra shown in figure 9 depend on the distance from the jet centreline at which they are calculated. For example inside the jet ($r/D=0$ or $r/D=0.5$), the main peaks are higher at inflow frequencies compared with the difference frequency; however, the supersonic tail is still the most energetic for the difference frequency.

3.2. *Alternative wave interactions*

Until now only interactions between axisymmetric ($n=0$) modes have been investigated. Bearing in mind that the growth rates of the axisymmetric ($n=0$) and first azimuthal ($n=1$) modes are similar, the interaction between first two azimuthal modes as well as that between the axisymmetric and first azimuthal modes is also expected to be important with respect to sound generation. The interaction between first two azimuthal modes generates an axisymmetric difference frequency spectral peak, and the interaction between axisymmetric and first azimuthal modes leads to a difference frequency with azimuthal wavenumber $n=1$ (or $n=-1$). Both azimuthal modes with $n=0$ and $n=1$ ($n=-1$) are known to be active in the acoustic far field. Inflow frequencies were chosen again such that the difference frequency $\Delta\omega$ would be maximally amplified. The results obtained were very similar to those presented earlier for the interaction between two axisymmetric waves: (i) the difference frequency dominates in the acoustic far field, (ii) sound radiation is mainly confined to the small angles from the jet downstream axis, and (iii) results are not very sensitive to the specific choice of the inflow frequencies, provided that both primary waves are highly amplified and the resulting difference frequency is somewhere within the range of the broadband peak (around $St\approx 0.22$). Therefore, we have chosen not to present the results here; more details may be found in Suponitsky & Sandham (2009).

3.3. *Interaction between two waves with azimuthal numbers $n=\pm 1$ ($-1/+1$ interaction)*

The interaction between two helical modes with the azimuthal numbers $n_1=-1$ and $n_2=+1$ is also of great interest with respect to sound radiation, as it generates a difference frequency spectral peak with azimuthal wavenumber $n=+2$ (or $n=-2$). This azimuthal mode has been found to be active in the acoustic far field of subsonic jets (e.g. Gamard, Jung & George 2004). Contributions to the sound from modes with azimuthal wavenumbers $n=\pm 2$ may come from a linear mechanism (direct radiation at low frequencies by instability waves with azimuthal wavenumbers $n=\pm 2$) and/or from the weakly nonlinear mechanism (radiation resulting from the interaction between two instability waves, e.g. two waves with azimuthal numbers $n_1=0$ and $n_2=2$ or with $n_1=-1$ and $n_2=+1$). The linear mechanism is unlikely to make a major contribution, as amplitudes and growth rates of the azimuthal modes $n=\pm 2$ near the nozzle exit are small for such low frequencies. The interaction between the modes with azimuthal wavenumbers $n=0$ and $n=2$ is also unlikely to be very efficient because of the large differences in the growth rates for these modes. Therefore, the main contribution to the noise coming from the azimuthal mode with $n=2$ is most likely to come from the interaction between the instability modes with azimuthal wavenumbers $n=\pm 1$. The relevance of such an interaction to the sound generation from the subsonic jet is also considered in the recent work of Wu & Huerre (2009).

Case	ω_1	n_1	ω_2	n_2	$\Delta\omega$	Δn	Co-flow (%)	A_{ij}
$C1\pm1$	2.4	−1	3.0	+1	0.6	2	10	5×10^{-4}
$C2\pm1$	2.4	−1	3.0	+1	0.6	2	10	1×10^{-4}
$C3\pm1$	1.8	−1	2.4	+1	0.6	2	10	5×10^{-4}
$C4\pm1$	2.2	−1	3.2	+1	1.0	2	10	5×10^{-4}
$C5\pm1$	2.4	−1	3.0	+1	0.6	2	1	1×10^{-4}

TABLE 3. List of runs for the interaction with azimuthal numbers $n=\pm1$.

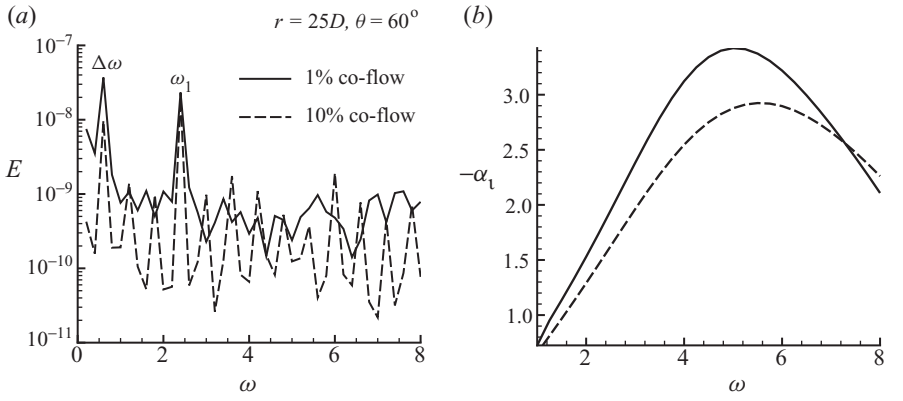

FIGURE 10. (*a*) Pressure fluctuations spectra calculated at $r=25D$ and $\theta=60^\circ$ for the simulations with the different amounts of co-flow, cases $C2\pm1$ and $C5\pm1$ in table 3; (*b*) growth rates $-\alpha_i$ versus frequency calculated from LST for the velocity profiles at $z/D=0$ with different amounts of co-flow.

The interaction between two helical modes with opposite azimuthal wavenumbers is known to be very efficient in causing transition to turbulence. As a result, simulations with an amplitude of the inflow disturbance large enough to cause significant nonlinear effects also lead to breakdown of the jet column into smaller structures. When this happens we cannot distinguish between the sound coming from instability waves and that radiated during the process of breakdown of the jet column into smaller structures. An additional undesirable side effect of the transition to turbulence is that because the pressure fluctuations lose their periodic behaviour, much longer times are required to accumulate converged statistics.

To overcome this problem, the co-flow was increased to 10 %. This reduces the disturbance growth rates and allows us to carry out simulations with the desired amplitudes of the inflow disturbances. The inflow frequencies were chosen close to the most amplified hydrodynamic frequency. The list of runs carried out for this kind of interaction is given in table 3. The effect of the co-flow on the amplitude of radiated sound is studied by comparing the results obtained for cases with different amounts of co-flow ($v_{coflow}=1\,\%$ and $v_{coflow}=10\,\%$, cases $C2\pm1$ and $C5\pm1$ in table 3). Pressure fluctuation spectra are shown in figure 10(*a*). It can be seen that the increase of the co-flow from 1 % to 10 % has a significant effect (approximately half an order of magnitude) on the amplitude of the difference frequency spectral peak at $\Delta\omega=0.6$. This can be explained by comparing growth rates calculated for the inflow velocity profiles ($z/D=0$) with different amounts of co-flow using LST (figure 10*b*). This figure shows that the amount of co-flow has a noticeable effect on the growth

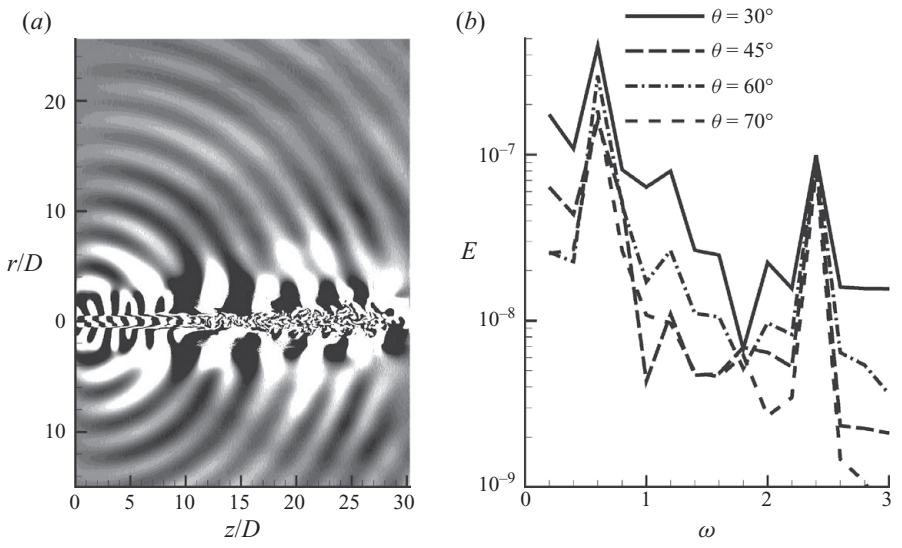

FIGURE 11. (*a*) Dilatation rate contours, contour levels -1×10^{-6} to 1×10^{-6}. (*b*) Pressure fluctuation spectra at radial distance $r=25D$ and different angles θ from the jet downstream axis. Case $C1\pm1$ in table 3 ($\omega_1=2.4$, $n_1=-1$ and $\omega_2=3.0$, $n_2=+1$).

rates, and therefore on the amplitude which a particular mode reaches during its downstream evolution. As such, with bigger co-flow, a higher amplitude of the inflow disturbance is required for the breakdown into turbulence to occur.

An instantaneous sound field is presented in figure 11(*a*) for the $C1\pm1$ case in table 3. One can see that the sound field obtained from the jet perturbed by two modes with azimuthal wavenumbers $n_1=-1$, $n_2=+1$ differs from that obtained when the jet is perturbed by two axisymmetric modes (compare figure 11*a* with figure 2*c*). The following differences can be observed between these results and those obtained with $n_1=n_2=0$: (i) perturbation of the jet by the pair of helical modes $n=\pm1$ leads to stronger side-line sound radiation; (ii) the peak sound radiation occurs at higher angles θ from the jet downstream axis, consistent with Wu & Huerre (2009); and (iii) the sound seems to originate closer to the inflow boundary (i.e. before the end of the potential core).

The pressure spectra calculated on an arc of radius $25D$ are shown in figure 11(*b*). As previously discussed, the difference frequency is dominant in the acoustic field, provided the amplitude of the inflow disturbance is sufficient to cause significant nonlinear effects. Following the variation of the amplitude with angle θ, we can see that the local maximum occurs in the vicinity of $\theta\approx60^\circ$, coinciding with the visual angle of the peak radiation (figure 11*a*). The maximum amplitude of the difference frequency occurs at $\theta=30^\circ$. However, it seems that at small angles there is an influence of the hydrodynamic near field that is responsible for the increase of the mode amplitude. The nonlinear nature of the difference frequency spectral peak can be seen from figure 12(*a*), which shows pressure spectra calculated with different amplitudes of the inflow disturbance (cases $C1\pm1$ and $C2\pm1$ in table 3). One can see that while the amplitude of the inflow frequency $\omega_1=2.4$ varies linearly with the amplitude of the inflow disturbance (approximately a factor of 5), the amplitude of the difference frequency ($\Delta\omega=0.6$) varies as the square of the inflow disturbance amplitude (approximately a factor of 25). Spectra corresponding to

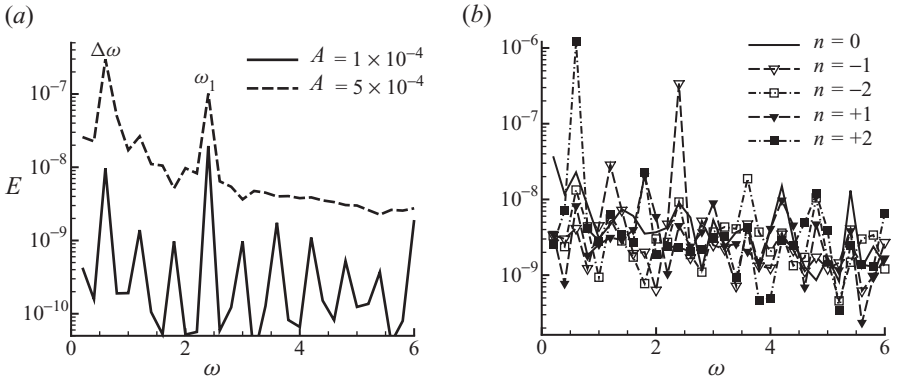

FIGURE 12. (*a*) Pressure fluctuation spectra calculated at $r = 25D$ and $\theta = 60°$ for two different amplitudes of the inflow disturbance, cases $C1 \pm 1$ and $C2 \pm 1$ in table 3. (*b*) Pressure fluctuation spectra calculated for several azimuthal modes at $r = 5D$ and $\theta = 45°$, $A = 5 \times 10^{-4}$.

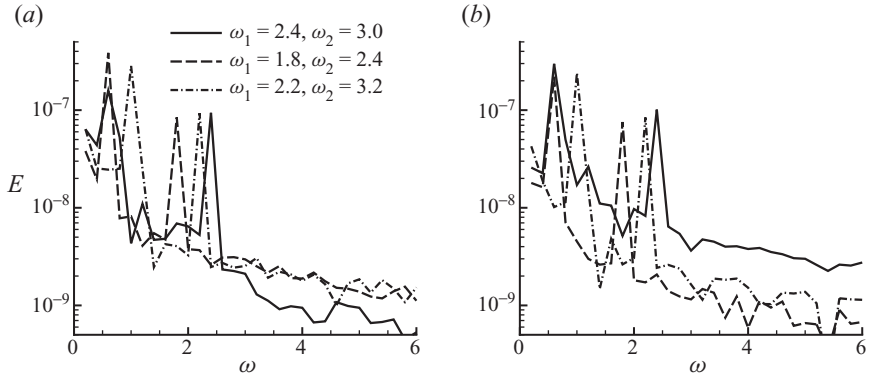

FIGURE 13. (*a*) Pressure fluctuation spectra calculated at radial distance of $r = 25D$ for the cases $C1 \pm 1$, $C3 \pm 1$ and $C4 \pm 1$ in table 3. (*a*) $\theta = 45°$; (*b*) $\theta = 60°$.

particular azimuthal modes are shown in figure 12(*b*) for the $C1 \pm 1$ case. It can be seen that the difference frequency $\Delta\omega = 0.6$ corresponds to the azimuthal mode $n = 2$, as expected from the interaction between two waves with $\omega_1 = 2.4$, $n_1 = -1$ and $\omega_2 = 3.0$, $n_2 = +1$.

It is also worth mentioning that the maximum sound radiation resulting from the interaction between two helical modes with $n = \pm 1$ seems to occur at lower frequencies of the difference mode in comparison with those obtained from the interaction between two axisymmetric ($n_1 = n_2 = 0$) or azimuthal ($n_1 = n_2 = +1$) modes. To demonstrate this, an additional simulation with $\Delta\omega = 1.0$ was carried out (case $C4 \pm 1$). Frequencies $\omega_1 = 2.4$ and $\omega_2 = 3.0$ as well as $\omega_1 = 2.2$ and $\omega_2 = 3.2$ were chosen to be centred around the most amplified hydrodynamic mode (based on LST calculations). To examine the effect of taking frequencies in a different range, an additional simulation with slightly lower frequencies but with the same $\Delta\omega$ was carried out (case $C3 \pm 1$). The results are presented in figure 13. In general, the amplitude of the difference mode is not significantly influenced either by increasing the frequency of the difference mode from $\Delta\omega = 0.6$ to $\Delta\omega = 1.0$ or by choosing the frequencies in a slightly different range

Case	Modes	A	Frequency	E_{fluc} at $r/D=0.5$
$C_n=0$	$n=0$	5×10^{-4}	0.2–7.0	2.124×10^{-6}
$C_n=1$	$n=+1$	5×10^{-4}	0.2–7.0	9.808×10^{-7}
$C_n=\pm1$	$n=\pm1$	5×10^{-4}	0.2–7.0	1.962×10^{-6}
$C_n=0\pm1$	$n=0,\pm1$	5×10^{-4}	0.2–7.0	4.086×10^{-6}
$C_n=0\pm1\pm2$	$n=0,\pm1,\pm2$	5×10^{-4}	0.2–7.0	6.385×10^{-6}
$C_n=0\pm1\pm2a$	$n=0,\pm1,\pm2$	1×10^{-4}	0.2–7.0	2.554×10^{-7}
$C_n=0\pm1\pm2b$	$n=0,\pm1,\pm2$	2×10^{-3}	0.2–7.0	1.022×10^{-4}

TABLE 4. List of runs for the interaction with azimuthal numbers $n=\pm1$.

($\omega_1=2.4$, $\omega_2=3.0$ or $\omega_1=1.8$, $\omega_2=2.4$). This result further indicates the broadband nature of low-frequency sound. It also shows that the results obtained are rather insensitive to the initial values, provided that these frequencies are highly amplified. A detailed examination of the results (figure 13) shows, however, some differences between the results with respect to the directivity of the radiated sound. It can be seen that in case $C1\pm1$, the radiation is stronger at $\theta=60^\circ$ in comparison to that at $\theta=45^\circ$ at radial distance $r=25D$. The situation is different for the $C4\pm1$ case, where the amplitude of the difference frequency mode is similar for both angles. Therefore, it seems that the amplitude of the radiated sound coming from the jet perturbed with two helical modes $n=\pm1$ remains nearly constant over the range of angles $\theta\leqslant70^\circ$. It is worth recalling that this result differs from that obtained earlier (interactions 0/0, 1/1 and 0/1), in which the radiated sound was mostly confined to small angles θ from the jet downstream axis.

Many additional interactions are possible. In Appendix A we consider a case in which the frequencies are integer multiplier of the difference frequency, but find no evidence for resonance. In Appendix B the difference in radiation patterns resulting from different kinds of nonlinear interactions is demonstrated by exciting the jet with three modes simultaneously.

4. Perturbation of the flow by a wide range of modes

In this section we present some results obtained from simulations in which the base flow was perturbed over a broad range of frequencies and with a range of azimuthal modes. The idea is to generalize the model of sound radiation based on the interaction between two primary instability waves that was studied in the previous sections and investigate how well the predictions of the sound field obtained by current approach compare with results obtained from DNS or experiments. For these simulations the initial disturbance is defined by $\tilde{u}=\sum_{i=1}^{N}\sum_{j=1}^{M}\mathrm{Re}\{A_{ij}\hat{u}_{ij}(r)\exp(i(n_j\Theta-\omega_i t+\phi_{ij}))\}$, where A_{ij} is the amplitude of a particular mode, $\hat{u}_{ij}(r)$ is an eigenfunction, n_j is the azimuthal mode number, ω_i is a real frequency and ϕ_{ij} is a randomized phase. For the simulations reported in this section a co-flow of 10 % was added to the jet. In all simulations the flow is perturbed for frequencies of $\omega_k=0.2k$, $k=1,35$, and each mode has the same amplitude $A_{ij}=A$. A list of simulations is given in table 4.

The spectra of pressure fluctuations calculated at $r=30D$ and $\theta=30^\circ$ are shown in figure 14(a) for the jet perturbed with different combinations of the azimuthal modes. (The interval between two subsequent frequencies is $\Delta\omega=0.2$ ($\Delta St=0.0318$), i.e. all points plotted correspond to excited frequencies.) One can see that for all cases the acoustic spectra feature a broadband low-frequency peak in the vicinity of $St\approx0.2$, in

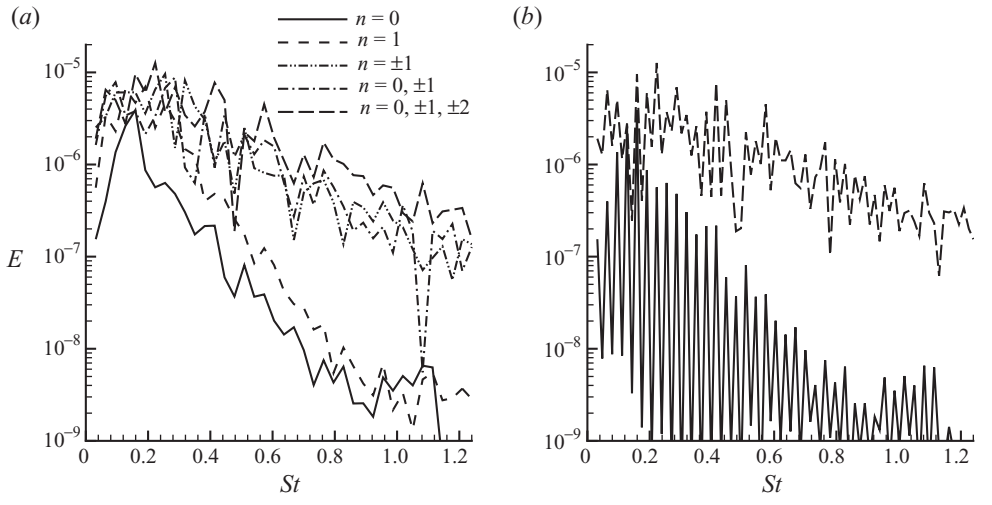

FIGURE 14. Spectra of the pressure fluctuations calculated at $r = 30D$ and $\theta = 30°$. (*a*) Effect of perturbing the jet with different combinations of azimuthal modes (only excited frequencies are shown), $A = 5 \times 10^{-4}$; (*b*) the spectra for cases $n = 0$ and $n = 0, \pm 1, \pm 2$ as in (*a*) but including frequencies which were not initially excited.

agreement with experimental and DNS results. For the $C_n = 0$ case (excitation by only axisymmetric modes) the peak is narrowest. This can be explained by the fact that only axisymmeric modes can be generated as a result of interactions between axisymmetric modes. This result also suggests that contributions from different interactions enter at slightly different frequencies, altogether generating a broadband peak.

At higher frequencies more significant differences between cases can be observed. When the jet is perturbed by only axisymmetric or first azimuthal modes, the high-frequency part of the spectrum is characterized by very rapid decay, whereas for the other cases ($C_n = \pm 1$, $C_n = 0 \pm 1$ and $C_n = 0 \pm 1 \pm 2$) the decay is much more gradual, and the overall shape of the spectra resembles that obtained in experiments. In the following we will show that this change in the behaviour of the high-frequency part of the spectrum can be attributed to whether or not the excitation by a particular combination of modes leads to a breakdown of the jet into smaller structure with ultimate transition to turbulence. Figure 14(*b*) shows the same spectra for cases $C_n = 0$ and $C_n = 0 \pm 1 \pm 2$, but with an interval between two subsequent frequencies $\Delta\omega = 0.1$ ($\Delta St = 0.0159$), i.e. including frequencies that are not initially excited. One can see that the spectrum for the $C_n = 0$ case is formed from discrete forced frequencies, whereas for the $C_n = 0 \pm 1 \pm 2$ case it is continuous. This indicates that there is a change in the flow field structure between the two cases.

To illustrate the change in the flow structure, figure 15 shows the sound and corresponding hydrodynamic fields. The sound field is shown by contours of the dilatation rate and the hydrodynamic field by contours of the vorticity magnitude. Figure 15(*a–d*) corresponds to the different cases in table 4: (*a*) $C_n = 0$, (*b*) $C_n = +1$, (*c*) $C_n = 0 \pm 1$ and (*d*) $C_n = 0 \pm 1 \pm 2$. One can see that for the cases in which the jet is excited by only axisymmetric or first helical modes (figure 15*a*, *b*), the sound field is characterized by low-frequency waves radiating mainly in the downstream direction. No side-line sound is observed in these cases. On the other hand, for the cases in which the jet is excited by a combination of azimuthal modes, the sound field is less organized and side-line radiation can be observed. Comparing vorticity

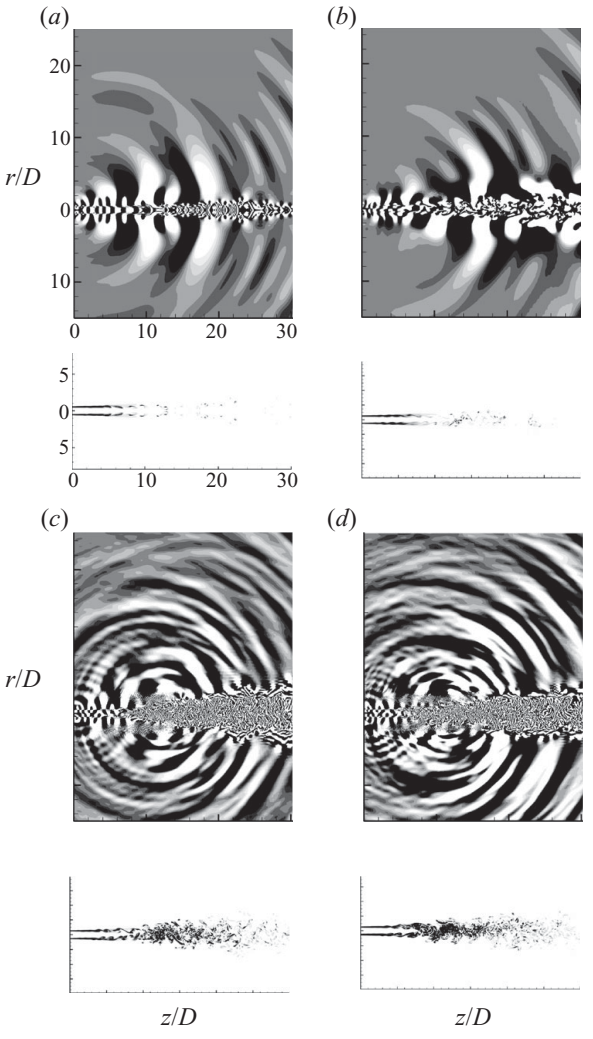

FIGURE 15. Contours of the dilatation rate and enstrophy. (*a*) $C_n = 0$; (*b*) $C_n = +1$; (*c*) $C_n = 0 \pm 1$; (*d*) $C_n = 0 \pm 1 \pm 2$ (see table 4). Contour levels are the same in all cases.

magnitude, the main difference between the results presented in figures 15(*a*) and 15(*b*) and those in figures 15(*c*) and 15(*d*) is whether the jet breaks down into smaller structures near the end of the potential core. These results clearly suggest that the low-frequency waves radiating in the downstream directions originate from primary instability waves (or more precisely interactions between them), whereas a significant portion of high-frequency sound at all angles comes from the breakdown of the large-scale structures near the end of the potential core.

Figure 16 shows the dilation rate obtained by excitation with the modes $n = 0, \pm 1, \pm 2$ and different amplitudes of the inflow disturbance: (*a*) $A = 1 \times 10^{-4}$ (case $C_n = 0 \pm 1 \pm 2a$) and (*b*) $A = 5 \times 10^{-4}$ (case $C_n = 0 \pm 1 \pm 2$). Figure 16(*c*) shows the dilatation rate obtained for the case in which the base flow is not maintained during the simulation, i.e. forcing terms are switched off. This simulation can be viewed as a DNS on a coarse grid with all other parameters the same as for figure 16(*b*). It can be seen that for the small amplitude inflow disturbance (figure 16*a*) the sound

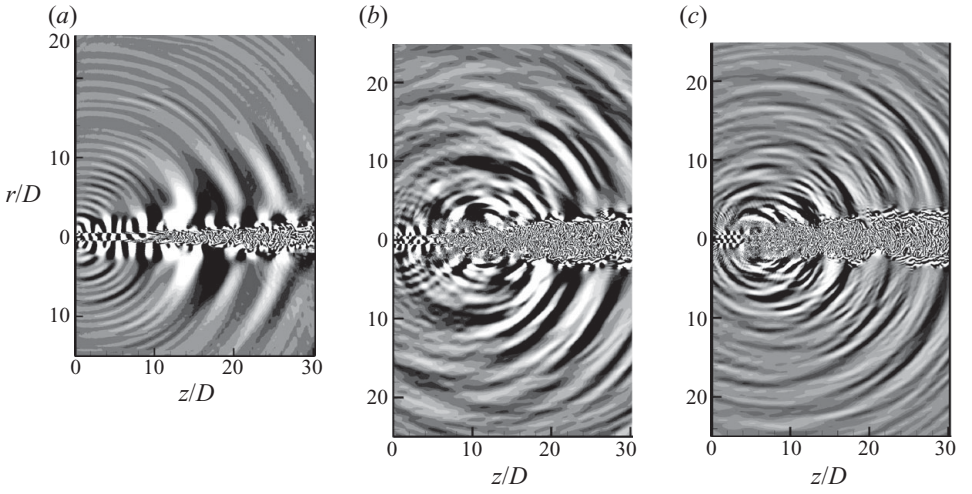

FIGURE 16. Contours of the dilatation rate: (*a*) case $C_n = 0 \pm 1 \pm 2a$ ($A = 1 \times 10^{-4}$); (*b*) case $C_n = 0 \pm 1 \pm 2$ ($A = 5 \times 10^{-4}$); (*c*) DNS on a coarse grid (base flow forcing terms are switched off), all other parameters are the same as in (*b*).

field consists of low-frequency waves radiated in the downstream direction and also of other waves originating close to the nozzle exit and radiating at higher angles from the jet centreline. Downstream sound comes mainly from interactions 0/0, 1/1 and 0/1 (or 1/0) considered in the previous sections, while the low-frequency sound radiated at higher angles comes from the interaction $-1/+1$. It is worth mentioning that no breakdown of the large structures is observed for the small amplitude of the inflow disturbance in figure 16(*a*). Comparing results for the higher amplitude of the inflow disturbance (figure 16*b*, *c*), we can see that the sound fields obtained with and without maintaining the base flow do not look very different, suggesting that the current approach captures important mechanisms of sound radiation from subsonic jets. When the base flow is maintained (figure 16*a*, *b*), some coherent high-frequency sound can be seen very close to the nozzle exit. This sound (which does not exist when the base flow is not maintained) appears to arise from a linear mechanism at the inflow boundary where LST modes, calculated using a parallel flow assumption, adjust to the non-parallel base flow.

Finally, figure 17 shows spectra of pressure fluctuations calculated at $r = 30D$ and $\theta = 30^\circ$ for different amplitudes of the inflow disturbance (figure 17*a*) and a comparison between the results obtained with and without maintaining the base flow during the simulation (figure 17*b*). Experimental data from Stromberg *et al.* (1980) are also added in figure 17*b*. Results are shown for the jet perturbed with modes $n = 0, \pm 1, \pm 2$, cases $C_n = 0 \pm 1 \pm 2$, $C_n = 0 \pm 1 \pm 2a$ and $C_n = 0 \pm 1 \pm 2b$ in table 4. In figure 17(*a*) a solid light grey line corresponds to the case with $A = 1 \times 10^{-4}$ multiplied by a factor of 25. One can see that, even with a small amplitude of the inflow disturbance (a weakly nonlinear case), the low-frequency broadband peak in the vicinity of $St \approx 0.2$ is well captured. Moreover, the amplitude of the radiated sound scales quadratically with the amplitude of the inflow disturbance (compare the solid light grey and dashed lines in figure 17*a*). This result is very important, as it clearly illustrates the nonlinear mechanism responsible for the sound radiation at these frequencies. Not much difference is observed for the simulations with bigger amplitudes of the inflow disturbances, as in these cases nonlinear effects are significant,

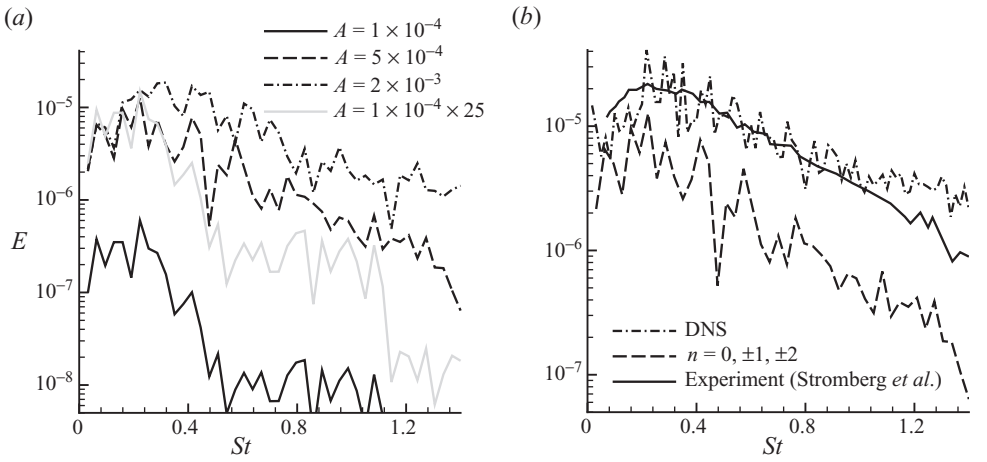

FIGURE 17. Spectra of the pressure fluctuations calculated at $r = 30D$ and $\theta = 30°$. (*a*) Effect of the inflow disturbance amplitude on the jet perturbed by mode $n = 0, \pm 1, \pm 2$. The light grey line corresponds to the case with $A = 1 \times 10^{-4}$ multiplied by a factor of 25; (*b*) comparison between the spectra obtained with (dashed line) and without (dash-dotted line) maintaining base flow during the simulation. Experimental data by Stromberg *et al.* (1980) are also shown (solid line).

resulting in nonlinear saturation. From the results presented in figure 17(*b*) we can see that the present approach provides a reasonable shape of the acoustic spectrum (in particular at low angles from the jet downstream axis). The shape of the spectrum is not very different for the simulations with and without maintaining the base flow.

5. Conclusions

Mechanisms of sound generation by instability waves have been investigated using numerical simulations. An important feature of the current work is that a base flow was prescribed using experimental data and maintained during the simulation. This approach allowed us to distinguish between linear and nonlinear mechanisms of sound radiation from instability waves. It also makes it possible to separate the sound originating from instability waves from that generated by small-scale structures.

The results demonstrate that low-frequency waves resulting from interactions between primary highly amplified instability waves can be efficient sound radiators in subsonic jets, further confirming earlier findings by Sandham *et al.* (2006*a*, 2008). It has also been shown that nonlinearly generated waves are more efficient in radiating sound compared with the instability wave at the same frequency originally existing in the flow. This was demonstrated by comparison of the energy content at supersonic phase velocities for the different kind of waves. Therefore, the frequency content of the near (hydrodynamic) field is not enough on its own to predict the radiated sound, as the origin of the frequency (linear, nonlinear) is also important. These results are in excellent agreement with the little-known experimental findings of Ronneberger & Ackermann (1979), who also reported the dominance of the difference frequency signal (resulting from the interaction between two primary axisymmetric waves) in the acoustic field of the turbulent round jet at lower Mach numbers.

The results show that interactions between two axisymmetric modes ($n_1 = n_2 = 0$) and between two helical modes $n_1 = n_2 = 1$ lead to highly directional sound fields confined mainly to small angles from the jet downstream axis. The interaction of

two helical modes ($n_1 = +1$, $n_2 = -1$) is also efficient with respect to the sound radiation. However, the radiated sound is still weaker than that produced by the 0/0 or 1/1 interactions. It was also found that the $-1/+1$ interaction leads to the sound radiation peaking at much higher angles from the jet downstream axis ($\theta \approx 60^\circ$) (in agreement with Wu & Huerre 2009). Simulations with the jet perturbed by a broad range of frequencies and combinations of azimuthal modes were also carried out. It was shown that these simulations capture a broadband peak at $St \approx 0.2$ at lower angles from the jet axis, suggesting that this low-frequency noise can be computed from the interaction model. The amplitude of the radiated sound was found to scale approximately quadratically with the amplitude of the inflow disturbance. This further confirms that the interaction between primary instability waves is the most relevant to the sound generation. A high-frequency noise seems to originate from the breakdown of the jet column into small-scale structures at the end of the potential core.

Appendix A. Additional calculations concerning potentially resonant inflow frequencies

In this appendix we consider two cases in which the inflow frequencies satisfy additional conditions that might lead to resonance effects. The first one is based on the observations from earlier that the interaction between frequencies $\Delta\omega$ and ω_1 (the lower inflow frequency) may generate a frequency $2\omega_1 - \omega_2$ that radiates sound efficiently into the far field (see figure 3*c*, *d* for $\omega = 1.0$) (cases *P*1a and *P*1b in table 1). Of interest is the situation in which this subsequent interaction will generate a mode at a frequency exactly equal to the difference frequency $\Delta\omega$. In the second case, we choose the inflow frequencies to be the fundamental (ω_1) and its first subharmonic ($\omega_1/2$). In this case the difference frequency resulting from the interaction between two waves will be exactly equal to the subharmonic ($\Delta\omega = \omega_1/2$ as in Laufer & Yen 1983) (cases *P*2a and *P*2b in table 1).

In the first case the jet was excited with $\omega_1 = 2.2$ and $\omega_2 = 3.3$ (cases *P*1a and *P*1b in table 1). These inflow frequencies give a difference frequency of $\Delta_{21}\omega = 1.1$. A subsequent interaction between this mode and the inflow frequency $\omega_1 = 2.2$ will generate a frequency $2\omega_1 - \omega_2 = \Delta_{21}\omega = 1.1$. It is worth mentioning that the present $\Delta_{21}\omega = 1.1$ is very close to the one used in § 3.1.1 ($\Delta_{21}\omega = 1.2$); therefore, in the absence of additional effects, we do not expect significant differences in the results as a consequence of a slight decrease in the value of $\Delta_{21}\omega$. The sound field for case *P*1b is presented in figure 18(*a*). It is very similar to that shown in figure 2(*c*), which was obtained for a jet excited with $\omega_1 = 2.2$ and $\omega_2 = 3.4$ for the same amplitude of the inflow disturbance. The spectra calculated at $r = 25D$ and $\theta = 30^\circ$ are shown in figure 18(*b*). It can be seen that (i) the amplitude of the difference frequency spectral peak is almost the same for cases *P*1b and *A*4 (compare the solid line at $\omega = 1.1$ with the dashed line at $\omega = 1.2$) and (ii) peaks at difference and inflow frequencies are narrower in case *P*1b (in comparison to *A*4), as the current choice of inflow frequencies limits the number of different frequencies which can be generated by nonlinear interactions. To summarize, it seems that the amplitude of the sound radiated at the difference frequency is not affected by this particular choice of inflow frequencies.

In the second case the jet was excited with ω_1 and $\omega_2 = \omega_1/2$ (cases *P*2a and *P*2b in table 1). The frequencies are chosen to give Δ_{21} reasonably close to those considered before, while the fundamental frequency ω_1 is highly amplified within a few diameters from the nozzle exit. These conditions are met by taking $\omega_1 = 2.8$ and $\omega_2 = 1.4$, which

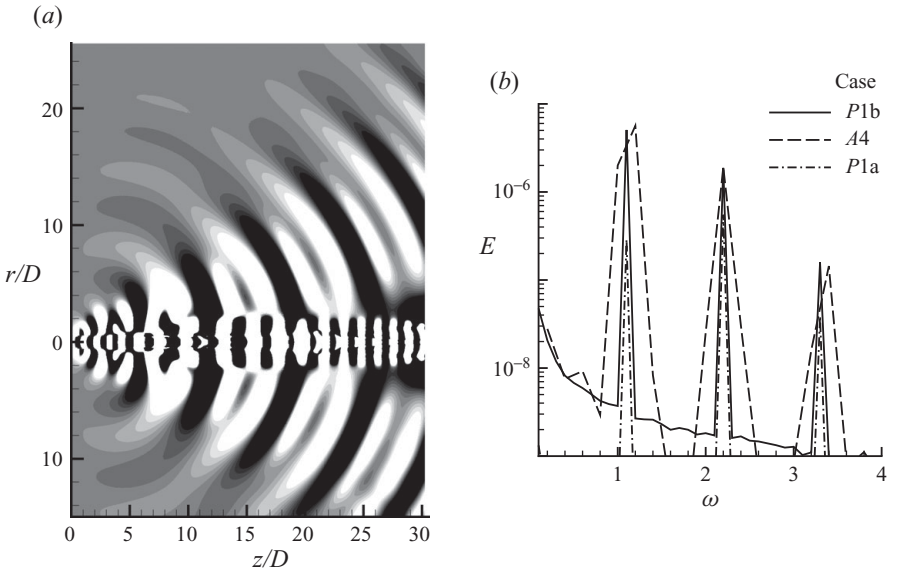

FIGURE 18. (*a*) Instantaneous dilatation rate contours for the case $P1b$ ($\omega_1 = 2.2,\ \omega_2 = 3.3,\ A = 5 \times 10^{-4}$). Contours are shown for the same levels as in figure 2(*c*). (*b*) Spectra of pressure fluctuations calculated at $r = 25D$ and $\theta = 30°$. Line styles: solid line, $\omega_1 = 2.2,\ \omega_2 = 3.3,\ A = 5 \times 10^{-4}$; dashed line, $\omega_1 = 2.2,\ \omega_2 = 3.4,\ A = 5 \times 10^{-4}$; dash-dotted line, $\omega_1 = 2.2,\ \omega_2 = 3.3,\ A = 1 \times 10^{-4}$.

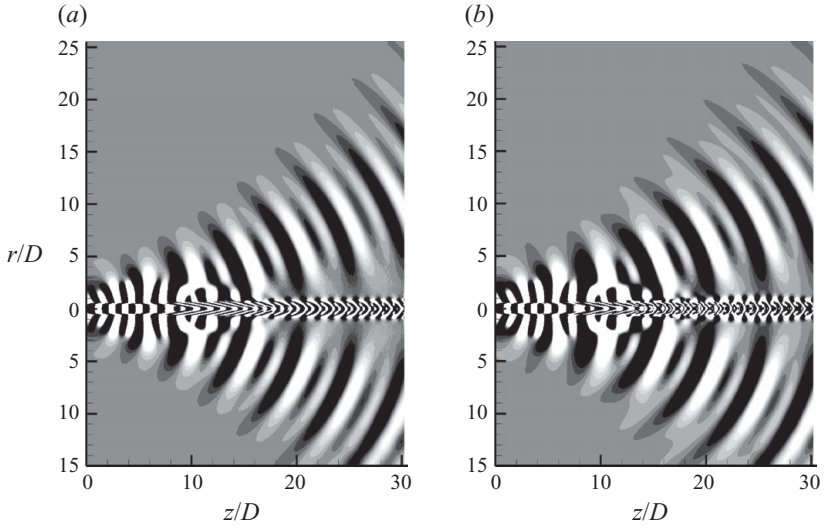

FIGURE 19. Dilatation rate contours for the jet perturbed at inflow frequencies $\omega_1 = 1.4$ and $\omega_2 = 2.8$, cases $P2a$ and $P2b$ in table 1. (*a*) Case P2a ($A = 1 \times 10^{-4}$). (*b*) Case $P2b$ ($A = 5 \times 10^{-4}$). For (*a*) and (*b*) contour levels are the same as in figures 2(*b*) and 2(*c*), respectively.

leads to a difference frequency $\Delta_{21}\omega = 1.4$. Figure 19 shows dilatation rate contours obtained for two different amplitudes of the inflow disturbances. One can see that the structure of the sound field remains almost the same for both amplitudes of the

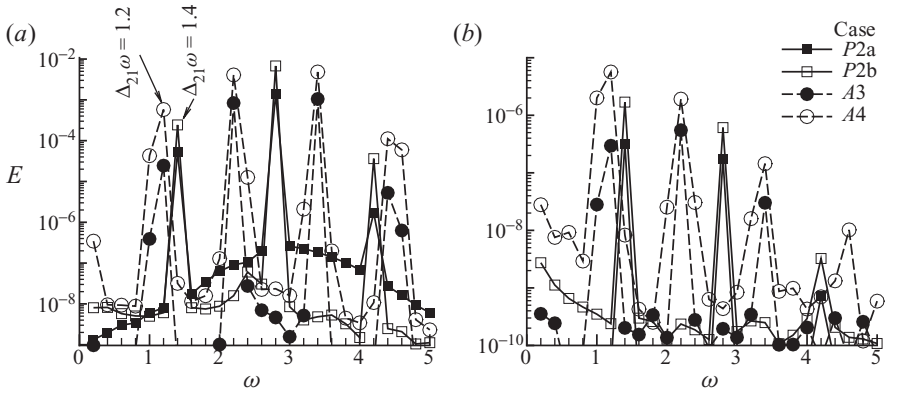

FIGURE 20. Spectra of pressure fluctuations calculated at (*a*) inside shear layer at $r/D = 0.6$ and $z/D = 5$; (*b*) at radial distance of $r = 25D$ and $\theta = 30°$. The solid lines correspond to forcing at $\omega_1 = 2.8$ and $\omega_2 = 1.4$ and the dashed lines correspond to forcing at $\omega_1 = 2.2$ and $\omega_2 = 3.4$; solid symbols are for $A = 1 \times 10^{-4}$ and hollow symbols are for $A = 5 \times 10^{-4}$.

inflow disturbance (compare figure 19*a*,*b* with figure 2*b*, *c*; in both figures contours are presented for the same levels).

To understand what is happening in this case, spectra are compared with those obtained with forcing at $\omega_1 = 2.2$ and $\omega_2 = 3.4$. Results are presented in figure 20(*a*) for a point inside the shear layer at $r/D = 0.6$ and $z/D = 5$, and in figure 20(*b*) for the sound field at a radial distance of $r = 25D$ and $\theta = 30°$. The near-field pressure spectra (figure 20*a*) suggest that this choice of inflow frequencies does not lead to significant amplification at the subharmonic frequency, i.e. 'subharmonic resonance' (see e.g. Cohen & Wygnansky 1987) does not seem to occur in this case. This can be seen by comparing amplitudes of the mode at $\omega = 1.4$ for the two cases with different amplitudes of the inflow disturbances (compare the solid lines with full and hollow square symbols). One can see that an increase of 5 times in the amplitude of the inflow disturbances leads to an increase of about 4.5 times in the amplitude of the spectral peak at $\omega = 1.4$; it appears that the subharmonic growth in this case is mainly governed by a linear mechanism. On the other hand, a nonlinear growth of the difference frequency spectral peak at $\Delta_{21} = 1.2$ resulting from the interaction between $\omega_1 = 2.2$ and $\omega_2 = 3.4$ is clearly seen, by comparing the two dashed lines with full and open circle symbols. The subharmonic frequency (difference mode at $\omega = 1.4$) dominates the acoustic field (figure 20*b*); however, the sound at this frequency is generated mainly by a linear mechanism (solid lines with full and hollow square symbols). This can now explain the similar structure of the sound fields seen in figures 19(*a*) and 19(*b*) – in both cases the sound is generated mainly by a linear mechanism. The above results indicate that the excitation of the jet at fundamental and subharmonic frequencies does not lead to enhanced sound radiation, in contrast to the results obtained for the jet excited by two highly amplified instability waves (frequencies of the difference mode in both cases are similar). However, it is worth emphasizing that the instability waves at inflow frequencies $\omega_1 = 2.8$ and $\omega_2 = 1.4$ have initially different phase velocities, and therefore the conditions for the subharmonic resonance (Cohen & Wygnansky 1987) are not exactly satisfied in this case. Therefore, the effect of a possible subharmonic resonance on the radiated noise remains to be investigated.

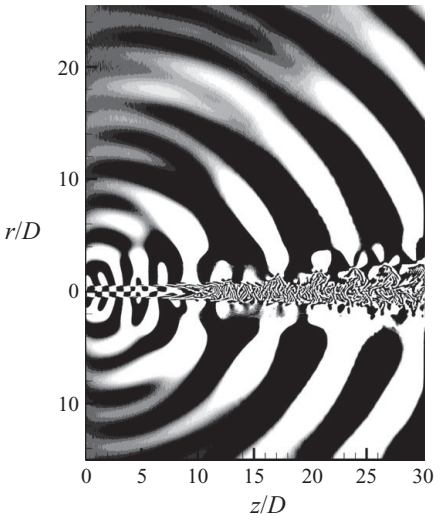

FIGURE 21. Instantaneous dilatation rate contours for the jet perturbed by the three modes simultaneously: $\omega_1 = 2.4$, $n_1 = -1$; $\omega_2 = 3.0$, $n_2 = +1$; $\omega_3 = 1.8$, $n = +1$; $A = 5 \times 10^{-4}$; co-flow = 10 %. (Contour levels are from -1×10^{-6} to 1×10^{-6}.)

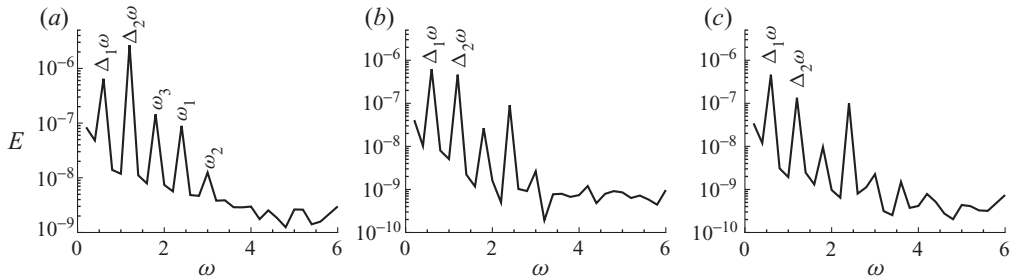

FIGURE 22. Spectra of pressure fluctuations calculated at radial position $r = 25D$ for the jet perturbed by three modes simultaneously ($\omega_1 = 2.4, n_1 = -1; \omega_2 = 3.0, n_2 = +1; \omega_3 = 1.8, n = +1; A = 5 \times 10^{-4}$; co-flow = 10 %). (*a*) $\theta = 30°$, (*b*) $\theta = 45°$ and (*c*) $\theta = 60°$.

Appendix B. Three-wave interactions

In this appendix we demonstrate how multiple wave interactions can be interpreted in terms of the two-wave interactions given in § 3. The jet was perturbed by the following combination of modes: $\omega_1 = 2.4$, $n_1 = -1$; $\omega_2 = 3.0$, $n_2 = 1$ and $\omega_3 = 1.8, n_3 = 1$, which leads to generation of two difference frequency spectral peaks: (i) $\Delta_1\omega = 0.6$, which results from the interaction between ω_1 and ω_2 or from the interaction between ω_1 and ω_3, having an azimuthal wavenumber $\Delta_1 n = 2$ or $\Delta_1 n = -2$, respectively; and (ii) $\Delta_2\omega = 1.2$, which results from the interaction between ω_2 and ω_3, with an azimuthal wavenumber $\Delta_2\omega = 0$ (i.e. axisymmetric). The inflow amplitude of each mode was taken as $A = 5 \times 10^{-4}$ and the amount of co-flow was 10 %. A snapshot of the dilatation rate field is shown in figure 21. One can distinguish the existence of two modes in the acoustic field: one which radiates predominantly in the downstream direction and is characterized by the shorter wavelength, and another one which radiates more side-line sound and has a longer wavelength. Pressure spectra calculated from these simulations at a radial distance $r = 25D$ and different angles θ are shown in figure 22. It can be seen that in the downstream direction ($\theta = 30°$,

figure 22*a*) the dominant frequency is $\Delta_2\omega = 1.2$. At $\theta = 45^\circ$ (figure 22*b*) both difference frequency spectral peaks have nearly equal amplitude, whereas at higher angles ($\theta = 60^\circ$, figure 22*c*) the difference frequency $\Delta_1\omega = 0.6$ becomes dominant. Spectra in the azimuthal direction (not shown) confirm that the frequencies $\Delta_1\omega = 0.6$ and $\Delta_2\omega = 1.2$ are associated with azimuthal wavenumbers $n = 2$ (or $n = -2$) and $n = 0$, respectively. The results demonstrate that the sound radiated by instability waves is not always confined to small angles from the jet downstream axis as usually assumed.

This work was funded by EPSRC grant EP/E032028/1. Computer time was provided by EPSRC via the UK Turbulence Consortium (grant EP/D044073/1).

REFERENCES

Cohen, J. & Wygnansky, I. 1987 The evolution of instabilities in the axisymmetric jet. Part 2. The flow resulting from interaction between two waves. *J. Fluid Mech.* **176**, 221–235.

Crighton, D. G. & Gaster, M. 1976 Stability of slowly diverging jet flow. *J. Fluid Mech.* **77**, 397–413.

Crighton, D. G. & Huerre, P. 1990 Shear layer pressure fluctuations and superdirective acoustic sources. *J. Fluid Mech.* **220**, 355–568.

Freund, J. B. 2001 Noise sources in a low-Reynolds-number turbulent jet at Mach 0.9. *J. Fluid Mech.* **438**, 277–305.

Gamard, S., Jung, D. & George, W. K. 2004 Downstream evolution of the most energetic modes in a turbulent axisymmetric jet at high Reynolds number. Part 2. The far-field region. *J. Fluid Mech.* **514**, 205–230.

Gaster, M., Kit, E. & Wygnanski, I. 1985 Large-scale structures in a forced turbulent mixing layer. *J. Fluid Mech.* **150**, 23–39.

Goldstein, M. E. 2001 An exact form of Lilley's equation with a velocity quadrupole/temperature dipole source term. *J. Fluid Mech.* **443**, 231–236.

Jones, L. E., Sandberg, R. D. & Sandham, N. D. 2008 Direct numerical simulations of forced and unforced separation bubbles on an airfoil at incidence. *J. Fluid Mech.* **602**, 175–207.

Laufer, J. & Yen, T. 1983 Noise generation by a low-Mach-number jet. *J. Fluid Mech.* **134**, 1–31.

Moore, C. J. 1977 The role of shear-layer instability waves in jet exhaust noise. *J. Fluid Mech.* **80**, 321–367.

Ronneberger, D. & Ackermann, U. 1979 Experiments on sound radiation due to non-linear interaction of instability waves in a turbulent jet. *J. Sound Vib.* **62** (1), 121–129.

Sandberg, R. D. & Sandham, N. D. 2006 Nonreflecting zonal characteristic boundary condition for direct numerical simulation of aerodynamic sound. *AIAA J.* **44** (2), 402–405.

Sandberg, R. D., Sandham, N. D. & Joseph, P. F. 2007 Direct numerical simulations of trailing-edge noise generated by boundary-layer instabilities. *J. Sound Vib.* **304**, 677–690.

Sandham, N. D., Li, Q. & Yee, H. C. 2002 Entropy splitting for high-order numerical simulation of compressible turbulence. *J. Comput. Phys.* **178**, 307–322.

Sandham, N. D., Morfey, C. L. & Hu, Z. W. 2006*a* Nonlinear mechanisms of sound generation in a perturbed parallel jet flow. *J. Fluid Mech.* **565**, 1–23.

Sandham, N. D., Morfey, C. L. & Hu, Z. W. 2006*b* Sound radiation from exponentially growing and decaying surface waves. *J. Sound Vib.* **294**, 355–361.

Sandham, N. D. & Salgado, A. M. 2008 Nonlinear interaction model of subsonic jet noise. *Phil. Trans. R. Soc.* A **366** (1876), 2745–2760.

Sandham, N. D., Salgado, A. M. & Agarwal, A. 2008 Jet noise from instability mode interactions. *AIAA paper* 2008-2987. 14th AIAA/CEAS Aeroacoustic Conference, Vancouver, Canada.

Sandhu, H. S. & Sandham, N. D. 1994 Boundary conditions for spatially growing compressible shear layers. *Rep.* QMW-EP-1100. Faculty of Engineering, Queen Mary and Westfield College, University of London.

Stromberg, J. L., McLaughlin, D. K. & Troutt, T. R. 1980 Flow field and acoustic properties of a Mach number 0.9 jet at a low Reynolds number. *J. Fluid Mech.* **72**, 159–176.

Suponitsky, V. & Sandham, N. D. 2009 Nonlinear mechanisms of sound radiation in a subsonic jet. *AIAA paper* 2009-3317. 15th AIAA/CEAS Aeroacoustic Conference, Miami, Florida, USA.

Suzuki, T. & Colonius, T. 2006 Instability waves in a subsonic round jet detected using a near-field phased microphone array. *J. Fluid Mech.* **565**, 197–226.

Tam, C. K. W. 2009 Mach wave radiation from high-speed jets. *AIAA J.* **47** (10), 2440–2448.

Tam, C. K. W. & Burton, D. E. 1984 Sound generated by instability waves of supersonic flows. Part 2. Axisymmetric jets. *J. Fluid Mech.* **138**, 273–295.

Tam, C. K. W. & Golebiowski, M. 1996 On the two components of turbulent mixing noise from supersonic jets. *AIAA paper* 96-1716. 2nd AIAA/CEAS Aeroacoustics Conference, State College, PA.

Tam, C. K. W. & Morris, P. J. 1980 The radiation of sound by the instability waves on a compressible plane turbulent shear layer. *J. Fluid Mech.* **99**, 349–381.

Tam, C. K. W., Viswanathan, K., Ahuja, K. K. & Panda, J. 2008 The sources of jet noise: experimental evidence. *J. Fluid Mech.* **615**, 253–292.

Thompson, K. W. 1987 Time dependent boundary conditions for hyperbolic systems. *J. Comput. Phys.* **68**, 1–24.

Viswanathan, K. 2004 Aeroacoustics of hot jets. *J. Fluid Mech.* **516** (2), 39–82.

Viswanathan, K. 2008 Investigation of noise source mechanisms in subsonic jets. *AIAA J.* **46**(8), 2020–2032.

Wu, X. 2005 Mach wave radiation of nonlinearly evolving supersonic instability modes in shear layers. *J. Fluid Mech.* **523**, 121–159.

Wu, X. & Huerre, P. 2009 Low-frequency sound radiated by a nonlinearly modulated wavepacket of helical modes on a subsonic circular jet. *J. Fluid Mech.* **637**, 173–211.